Detection of Fracture Networks and Faults Based on Multiply Scattered Waves

by
Yinshuai Ding

A dissertation submitted to the Department of Earth and Atmospheric Sciences,

College of Natural Sciences and Mathematics

in partial fulfillment of the requirements for the degree of

Doctor of Philosophy
in Geophysics

Chair of Committee: Hua-Wei Zhou

Co-Chair of Committee: Yingcai Zheng

Committee Member: Leon Thomsen

Committee Member: Jonathan Liu

University of Houston
December 2019

ACKNOWLEDGMENTS

I am fortunate to have found Dr. Hua-Wei Zhou and Dr. Yingcai Zheng as my advisors who have such a broad and deep knowledge in the field of geoscience. Without their constant help and guidance, I cannot reach where I am today. They will always encourage me to take positive actions in both research and life. Due to their patience in me, I can have enough time to dive in the area of geophysics and make improvements.

I would like to give my sincere thanks to my committee members, Dr. Leon Thomsen, and Dr. Jonathan Liu for their help and suggestions on my dissertation. As a TA in the summer short course and the professional master course taught by Dr. Leon Thomsen, I benefited a lot from his teaching on seismic anisotropy and wave propagation.

I would like to express my gratitude to all experts who have taught me about geophysics; it is their sharing of knowledge that leads me to a deeper understanding of geoscience. I have high respect for those researchers who make their research reproducible via software like Madagascar, Seismic Unix, CREWES Matlab, etc. Without their willingness to share their research, I could be in the darkness of seismic data processing.

I also want to express my great graditude to the Department of Earth and Atmospheric Sciences at University of Houston for the support of my PhD study. The staff have helped me so much to make my study go smoothly. My special thanks go to Karen Maldonado and Jay Krishnan for all the help they have offered me.

During the time of pursuing my PhD degree at UH, I have made many good friends. To name a few, they are Jingjing Zong, Keyao Xia, Yuandi Gan, Zhili Wei, Yukai Wo, Zhonghan Liu, Shuhang Tang, Boming Wu, Zhehao Li, Jiaxuan Li, Yuan Tian, Hao Hu, David Li, Yang Wang, Dan Li, Yijing Li, Yuchen Wu, Felix Gamez, Wanli Li. With their friendship, the time spent in Houston was more fun.

Finally, my deepest thanks go to my parents Wenzhi Ding and Guilong Fu, and my younger sister Chengyuan Ding. Without their unconditional love and support, I could not have achieved what I have accomplished now.

ABSTRACT

Fractures and faults are widely seen in nature. They can play important roles as storage for natural resources, paths for the migration of fluids including hydrocarbons, structural traps for petroleum reservoirs. Fracture characterization and fault imaging by using seismic methods have contributed greatly in finding economic reservoirs. In this dissertation, we focus on how to use multiply scattered waves to characterize fractures and image the faults.

The first part of the dissertation focuses on the fracture characterization using the Gaussian wave packet (GWP). Conventionally, using seismic anisotropy to study fractured media has gained great success in the cases where the effective medium theory (EMT) holds. As a supplement to EMT, our proposed method characterizes the fractures using multiply scattered waves when the EMT is no longer valid.

In our proposed method, we use a GWP which approximates as a local plane wave to interact locally with the fractured medium. The resultant multiply scattered waves can be used to characterize fractures in terms of spacing, compliance and orientation. We first study the propagation of the GWP to investigate how well it behaves as a local plane wave relative to the propagating distance and heterogenous velocities. Then, we describe how to build the GWP wavefield from the wavefields of point sources. Finally, we develop the method to characterize fractures. Using numerical examples, we show the potential usefulness of our method in fracture characterization.

The second part of the dissertation is concentrated on imaging high-angle faults using multiply scattered waves. When the faults have high angles, the directly reflected waves from fault planes need a longer offset to be recorded. However, a longer offset may not be favorable in practice.

Traditionally, the high-angle faults are interpreted and/or extracted by attributes but not imaged directly. With a limited offset, we aim at using multiply scattered waves to image the high-angle faults directly.

To fulfill the goal of imaging faults directly, we develop the asymmetrical reverse time migration (asym-RTM) algorithm. The asym-RTM images the sub-horizontal reflectors in its first iteration. Then, the imaged reflectors are added into the velocity model for the second iteration. In this way, we can utilize the second-order scattered waves to image the faults directly.

TABLE OF CONTENTS

LIST OF FIGURES

1 Introduction

1.1 Motivation and objectives

Conventional seismic imaging methods have gained great success in imaging the sub-horizontal geological structures. When the task is to characterize fracture networks (Trice, 2014) or image steep fault planes (Hale, 2013a) underground (Figure 1.1), the conventional methods may have limitations. The reason is twofold. First, the conventional imaging methods use only primary waves to form an image. Second, multiply scattering waves generated from fracture networks and fault planes are removed as noise within the framework of conventional imaging methods.

To characterize fracture networks, seismic anisotropy analysis such as shear wave splitting (Crampin, 1985) and amplitudes variation versus azimuth (Thomsen, 1995) is only viable when the fractured medium can be treated as an effective medium. However, due to the unevenness in fracture spacing and the effect of fracture clustering, the effective medium theory may be violated (Fang et al., 2017). Other imaging methods try to focus the diffracted waves and produce fracture images. Such a diffraction imaging method only works when the fractures are sparsely distributed, and the diffracted waves from individual fractures do not generate strong interference patterns.

For delineation of faults, the high-angle faults are traditionally treated as lateral reflection discontinuities in a processed migration image. By calculating seismic attributes to estimate the reflection continuities or discontinuities (Hale, 2013b), the fault planes are picked out by the calculated attributes. Based on the theory of image segmentation, fault delineation has been done by using machine learning algorithms (Wu et al., 2019). All these methods attempt to detect the fault locations from the processed images. The high-angle faults are not imaged directly in the same way as the sub-horizontal reflectors are imaged.

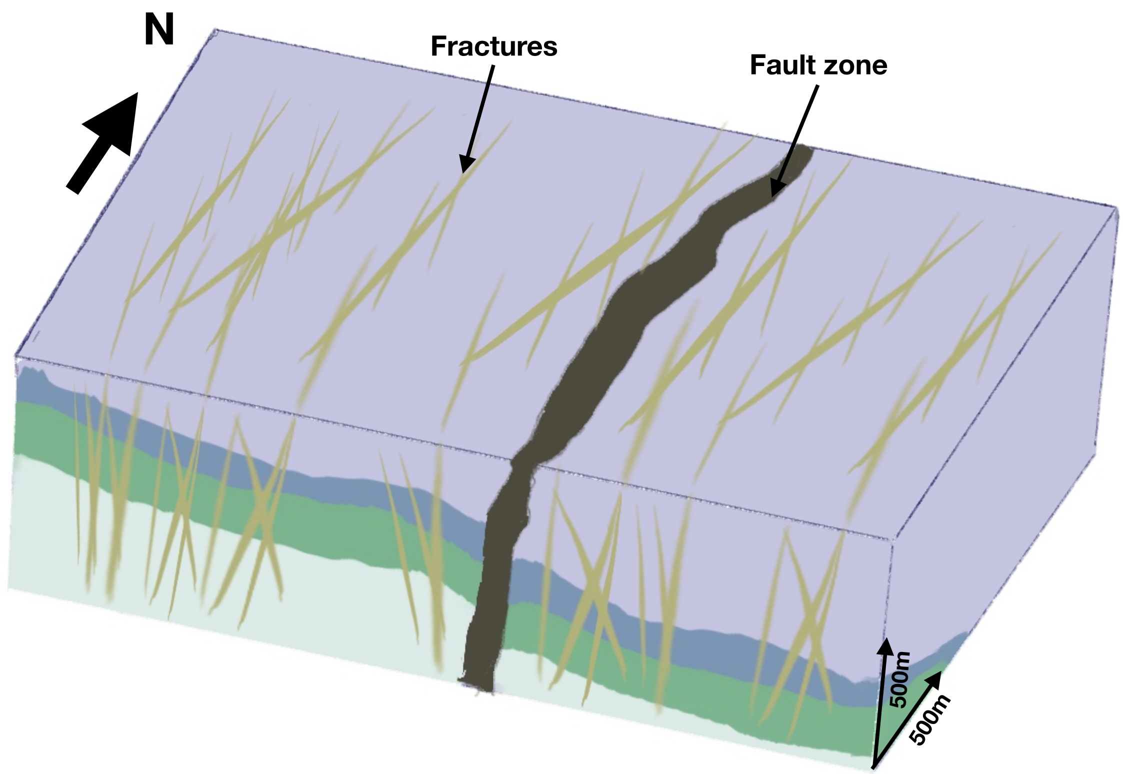

Figure 1.1: Schematic 3D fracture networks and fault underground, modified from Trice (2014).

Our research is to develop new techniques to enrich and enhance characterizing fractures and imaging steep fault planes in the subsurface. For fracture characterizations, we focus on using multiply scattered waves from the fracture networks to characterize them in a local sense. Under the scope of plane wave scattering theory, we use the Gaussian wave packet (Perel and Sidorenko,

2007) to represent a local plane wave and interact with fractures. The resultant scattered waves carry information (spacing, orientation, compliance) of fractures underground by forming specific scattering patterns in the time-distance domain (Zheng et al., 2013). For steep fault imaging, we propose a new method that directly exploits multiply (second-order) scattered waves from the fault planes to image faults. The application of multiply scattered waves is achieved by adding existing reflectors derived from the migration image into the previous velocity model. The added reflector is the key factor in imaging the target fault with the second-order scattered waves for the proposed imaging method.

1.2 Dissertation overview

In this dissertation, we apply multiply scattered waves to fracture characterizations and fault imaging. The dissertation is divided into two parts. The first part is to characterize fracture networks. We exploit the Gaussian wave packet (GWP) to characterize the fracture networks. The second part is to image fault planes by a new imaging algorithm that utilizes the second-order scattered waves reflected from the fault planes.

In the part on fracture characterizations, we study the Gaussian wave packet (GWP) propagation in different velocity media and the construction of GWP from point-shot gathers. To use the GWP in characterizing the fractures, we propose a new algorithm based on the method proposed by Zheng et al. (2013).The feasibility of the algorithm is exemplified by numerical simulations.

In the part on fault imaging, the conventional reverse time imaging (RTM) method (Baysal et al., 1983) lays the foundation for our new method: the asymmetrical RTM (asym-RTM). In the asym-RTM method, the multiply scattered waves are implemented in forming the steep fault image directly.

1.3 Dissertation outline

In Chapter 1, a general introduction of the dissertation is given.

In Chapter 2, the GWP is reviewed in its analytical formula and its propagation in the heterogeneous media is studied through numerical modelling.

In Chapter 3, the process of constructing a GWP record from point-source shot records is given. The effects of source interval and white noise on the construction of GWP records are discussed.

In Chapter 4, the fracture characterizations are done by using GWP. The multiply scattered waves due to the interactions between fractures and the incident GWP are studied for characterizing the fractures.

In Chapter 5, the RTM imaging method is reviewed first for conventional imaging. Then the asymmetrical RTM imaging method is proposed to image fault planes directly.

In Chapter 6, a summary of this dissertation is presented and future work is proposed.

2 Propagation of Gaussian wave packet in 2D heterogeneous media

2.1 Introduction

In the study of wave propagation, knowing both the location and the propagation direction of the wavefield is of great importance in seismic imaging and data processing. It is known that the seismic illumination (Xie et al., 2006) and angle coverage (Yan and Xie, 2010) are two key factors to get a high-quality imaging of the subsurface target. The beams and packets extracted from the seismic wavefield are good candidates to study the target area with focused illumination and different incident angles. Many researchers (e.g., Hernández-Figueroa et al., 2007) have studied how to propagate the wavefield locally and directionally by representing the whole wavefield with packets or beams.

Popov (1982) and Červenỳ et al. (1982) used the Gaussian beams (GB) to calculate the wavefield asymptotically in smoothly heterogeneous media. Later, Hill (1990) applied GB to seismic depth migration due to its fast computation and ability to handle caustics. Though GB are beam-like solutions localized in the Gaussian manner in the direction transverse to the ray, they are not localized along the ray because the GB is not localized in time. Babich and Ulin (1984) and Ralston (1982) discussed Gaussian packets as the building blocks of wave field. Gaussian packets (GP) has a similar expression (Klimeš, 1989) as GB but it is time-localized. GP and its application in seismic migration in common-shot domain were discussed by Žáček (2004). To better represent seismic data sparsely and accurately, Geng et al. (2014) introduced the Gabor-frame-based GP decomposition. Initially, GP can have a good localization in both space and propagation direction at time zero, it will quickly expand and diverge during propagation.

Since the concept of compressive sensing emerged, curvelets have been used to represent image data sparsely in digital signal processing (Candès et al., 2006). Geophysicists also used curvelets to represent seismic data sparsely and related them to Kirchhoff depth migration in the asymptotic sense (Douma and de Hoop, 2007). Besides curvelets, other wavelets are developed to represent seismic data too. Wu et al. (2008)constructed dreamlets based on a tensor product of beamlet (space localization) and drumbeat (time localization). The purpose is to get simultaneous time-space localization for seismic wave propagation and imaging. For the dreamlet, its time-space localization can only be maintained for a short propagation distance. Thus, after propagation through several depth intervals, the wavefield may need to be recomposed and decomposed again.

Different from all wave packets mentioned above, the Gaussian wave packet (GWP, not to be confused with GP) is an exact solution to the homogeneous wave equation (Kiselev and Perel, 1999, 2000; Kiselev, 2003, 2007; Perel and Sidorenko, 2007). Though the GWP is provided by its analytical formula in the homogeneous media, we can propagate it in any heterogeneous media by the finite difference method. Based on a set of proper parameters, the GWP can maintain its localization and direction in space over a long distance propagation in heterogeneous media (Zheng et al., 2011).

2.2 Review of GWP as a localized solution to the homogeneous wave equation

Considering the scalar wave equation in the two-dimensional infinite homogeneous medium, it describes a pressure wavefield $u(t,\mathbf{x})$ in time and space domain $\mathbf{x} = (x,z)$

$$\frac{\partial^2 u}{\partial t^2} - c^2(\frac{\partial^2 u}{\partial x^2} + \frac{\partial^2 u}{\partial z^2}) = 0 \tag{2.1}$$

where c is the constant wave propagation speed. The most common solution to Eq. 2.1 is the plane wave $u(t,\mathbf{x}) = g(t - \mathbf{r}\cdot\mathbf{x}/c)$ where g is a function representing the wavelet and $\mathbf{r}$ is the unit vector along the propagation direction.

Though the plane wave has a unique propagation direction indicated by the vector $\mathbf{r}$, the wavefield is infinite in space perpendicular to the propagation direction.

Different from the plane wave solution, the GWP (Perel and Sidorenko, 2007) solution has a finite size in space and a well-defined propagating direction:

$$u(t,\mathbf{x}) = \sqrt{\frac{\pi}{2}}\frac{(ps)^{\upsilon}K_{\upsilon}(ps)}{\sqrt{z+ct-i\varepsilon}}, \mathbf{r} = (x,z) \tag{2.2}$$

in which

$$s = \sqrt{1 - i\theta/\gamma} \tag{2.3}$$

and

$$\theta = z - ct + \frac{x^2}{z+ct-i\varepsilon} \tag{2.4}$$

where K_{υ} is the modifed Bessel function of the 3^{rd} kind, and υ is a real number which is chosen as 0.5 for its wavelet transform analysis (Perel and Sidorenko, 2007). Eq. 2.2 describes a GWP that propagates along the z direction. Since the solution is complex-valued, both the real and imaginary parts satisfy the wave equation (Eq. 2.1), seperately. Because the variable t is differentiated two times in the wave equation, the GWP can propagate from negative infinity to positive infinity in time or vice versa. The GWP can even be treated as a wavelet, and it still satisfies the wave equation with the wavelet transform (dilation, rotation, translation) (Perel and Sidorenko, 2007).

2.2.1 Propagation of GWP in homogeneous media

The GWP's geometric shape is controlled by three positive parameters (p, ε, γ), and its propagation direction and center location can be set by a rotation and a translation applied to the original GWP in space (Figure 2.1). Qualitatively, $\sqrt{p}$ indicates the number of oscillations in the wave packet along the longitudinal direction (i.e., the propagation direction); γ controls the packet spatial width in the longitudinal direction; γ/ε is the aspect ratio of the longitudinal dimension over the transverse dimension.

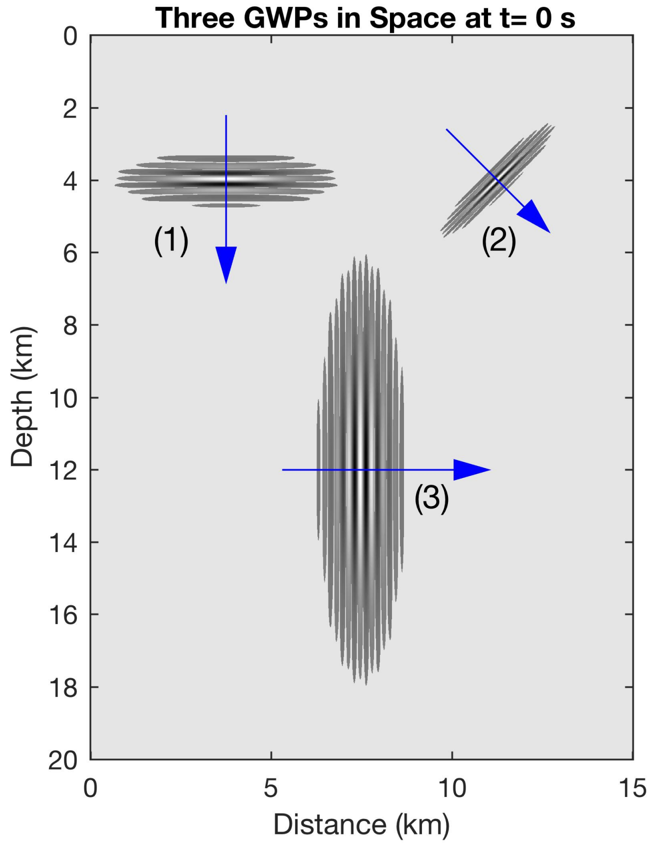

Figure 2.1: Three different GWPs with propagation indicated by arrows: (1) The GWP constructed with parameters $p = 16, \gamma = 0.4, \varepsilon = 40$. (2) The GWP constructed with parameters $p = 16, \gamma = 0.2, \varepsilon = 40$. (3) The GWP constructed with parameters $p = 64, \gamma = 0.4, \varepsilon = 40$.

The analytical GWP (Eq. 2.2) takes an asymptotic form when $p \gg 1$, $\gamma \leq \varepsilon$ and $2ct/\varepsilon =$O(p^{-l}), $1/3 < -l < 1/2$. We call this form the "rigid-motion" asymptotic solution:

$$u(t, \mathbf{x}) \sim exp[ik(z-ct) - \frac{(z-ct)^2}{2\sigma_z^2} - \frac{x^2}{2\sigma_x^2}] \tag{2.5}$$

where

$$k = p/(2\gamma), \sigma_z^2 = 4(\gamma)^2/p, \sigma_x^2 = \gamma\varepsilon/p \tag{2.6}$$

The essential support area of this asymptotic solution is an ellipse (when $\sigma_z \neq \sigma_x$) in space with the following aspect ratio:

$$e = \sigma_z/\sigma_x = 2\sqrt{\gamma/\varepsilon} \tag{2.7}$$

The packet propagates along the z-direction in Eq. 2.1, which can be defined as any direction. The packet amplitude profile forms a 2D Gaussian shape in space and it does not broaden in propagation.

The GWP is related to the Gaussian packet (GP), a widely used form in seismic imaging (Žáček, 2004; Geng et al., 2014) when $p \gg 1,\ \gamma > \varepsilon$ and $2ct/\varepsilon > 1$:

$$u(t,\mathbf{x}) \sim exp[ik(z-ct) - \frac{(z-ct)^2}{2\sigma_z^2} - \frac{x^2}{2\tilde{\sigma}_x^2} + i\frac{2ctkx^2}{4c^2t^2+\varepsilon^2}]\frac{C}{\sqrt{2ct-i\varepsilon}} \tag{2.8}$$

where

$$\tilde{\sigma}_x^2 = \sigma_x^2(1+4c^2t^2/\varepsilon^2) \tag{2.9}$$

In this case, the transverse packet width ($\tilde{\sigma}_x$) increases with propagation time. The phase front is parabolic in the transverse direction, similar to the Gaussian beam (Červenỳ et al., 1982; Popov, 1982).

With numerical examples, we show the propagation of several GWPs based on different choices of parameters $e = \sigma_z/\sigma_x,\ \sqrt{p},\ \sigma_z$ (Zheng et al., 2011) (Figure 2.2). The medium is homogeneous and 1.5 km/s. If we fix the GWP longitudinal dimension σ_z and the number of oscillations $\sqrt{p}$ in the longitudinal direction, the wave packet is diffraction-resistant when the packet aspect ratio e is small (Figure 2.2a & c). The packet shows a better localization and directionality when $\sqrt{p}$ is large while e, σ_z are fixed (Figure 2.2a & b). We note that the curvelet in Candès et al. (2006)

only has one oscillation. If we only vary σ_z, a smaller σ_z will give a more localized and directional GWP when keeping the other two factors fixed (Figure 2.2a & d).

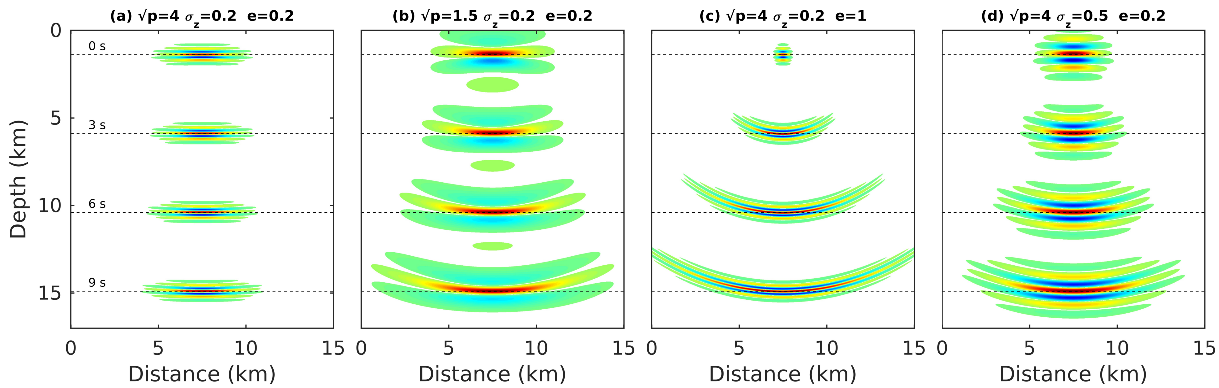

Figure 2.2: Four GWPs based on different parameters propagating vertically in a constant velocity model (1.5 km/s), and their wavefield snapshots at four time steps (0 s, 3 s, 6 s, 9 s) are shown in space.

2.2.2 GWP data recorded in homogenous media

When we create a GWP with a set of (p, ε, γ) in space at time 0 s by Eq. 2.2, the velocity c will not influence its packet shape. We show the same GWP propagating horizontally in two different constant velocity models (Figure 2.3). The GWPs in these two media keep the same overall shape at the same distance, but with different arrival times controlled by the velocity. The compactness of GWP is roughly symmetrical across time 0 s. We also record the data with vertically arranged receivers at the same horizontal location 0 km in the two media. The data recorded in the medium with velocity 1 km/s shows a broader packet shape along the time axis than the GWP data in the other medium (5 km/s) (Figure 2.4a & b). The broader packet means that the data has lower frequency (f) content (Figure 2.4c & d). Since the frequency (f) content in the data is related to both the medium velocity (c) and the wavelength (λ) by the equation $f = \lambda/c$. Thus, for the same GWP propagating with different velocities, we need sample it correctly in the time domain to avoid artifacts (Jerri, 1977).

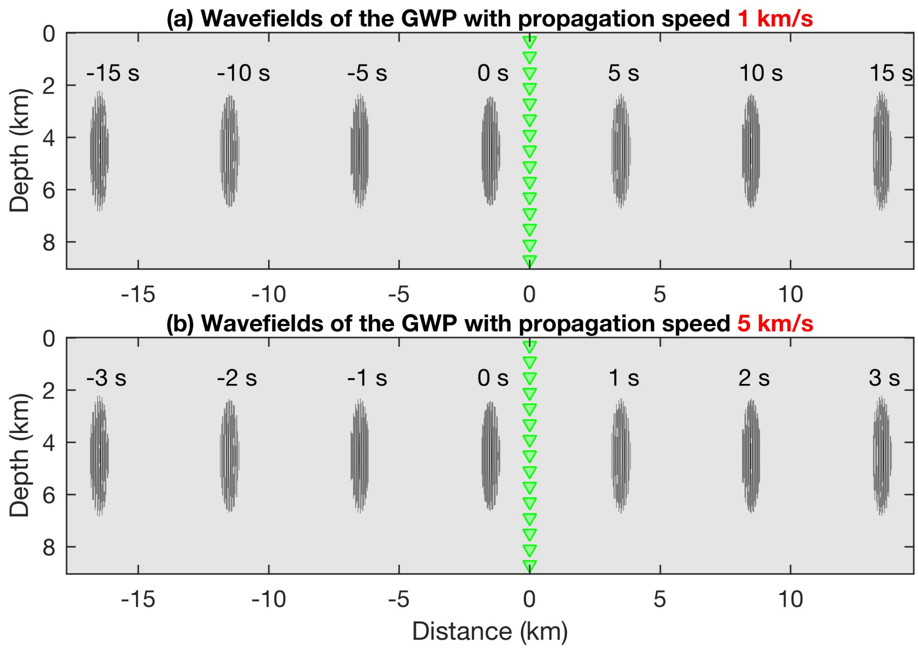

Figure 2.3: The GWP ($p = 81, \gamma = 0.5, \varepsilon = 80$) propagating horizontally in two different media, with receivers vertically arranged at the horizontal location 0 *km*. (a) Its wavefield at seven time steps (-15, -10, -5, 0, 5, 10, 15 *s*) in the constant velocity model (1 *km*/*s*). (b) Its wavefield at seven time steps (-3, -2, -1, 0, 1, 2, 3 *s*) in the other constant velocity model (5 *km*/*s*).

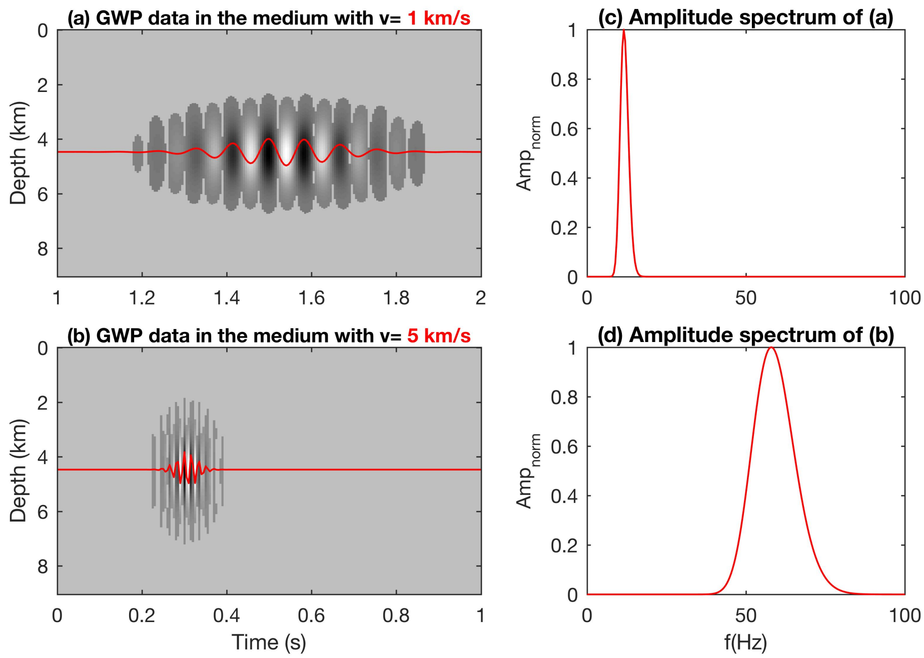

Figure 2.4: Data recorded at receivers in Figure 2.3. (a) GWP data recorded in receivers from Fig. 2.3a. (b) GWP data recorded in receivers from Fig. 2.3b. (c) Normalized amplitude spectrum of the red trace in (a). (d) Normalized amplitude spectrum of the red trace in (b).

2.3 Propagation of GWP in heterogeneous media

The original GWP solution (Kiselev and Perel, 2000; Perel and Sidorenko, 2007) was proposed for a homogeneous medium and can achieve the desired properties (localized in space and directional). It is unclear whether these desired properties can still exist for a GWP in heterogeneous media. To investigate this question, we use a finite-difference numerical method (FD, 2nd order accuracy in time and 4th order in space) to propagate a GWP into a heterogeneous medium with all absorbing boundaries (Moczo, Kristek, and Halada, Moczo et al.; Zhou, 2014).

In the model, we add a top homogeneous layer in which the GWP is initialized using the analytical solution. The input for the FD algorithm is the analytical GWP wavefields in the top layer at the first two time steps ($t_1 = 0s$, and $t_2 = \delta t s$, where δt is the time discretization step of the FD) and the velocity model. Then, the FD method can evolve the wavefield in time in the whole model (including the heterogeneous part). The GWP represented by Eq. 2.2 is complex-valued, but our modeling uses only the real part. In the following, we show three numerical examples for different complex media.

Case 1: **Reflection and transmission of a GWP**

Our first model is a two-layered velocity medium. The GWP ($p = 64, \gamma = 0.6, \varepsilon = 40$) is incident on the interface with an incidence angle of 30° (Figure 2.5a). The wave packet behaves as a particle traveling along the straight seismic ray. When it hits the interface, it splits into a reflected packet and a transmitted packet (Figure 2.5a).

Case 2: **GWP in a gradient medium**

The second medium is a homogenous layer atop a gradient layer (Figure 2.5b). The propagating GWP ($p = 36, \gamma = 0.6, \varepsilon = 40$) is localized along the curved seismic raypath in the gradient layer. The shape of the packet is being constantly distorted during propagation, especially at the turning point. However, the GWP reclaims its original shape when it returns to the top homogeneous layer. This is in sharp contrast with the traditional GB whose beam front usually diverges quickly and will not reconstruct to its original shape.

Case 3. **GWP in a random medium**

The third medium is a homogenous layer overlaying a smooth Gaussian random layer (Figure 2.5c) (Zheng and Wu, 2008). The shape of the GWP ($p = 36, \gamma = 0.6, \varepsilon = 40$) becomes distorted as it goes through the random heterogeneities. However, the packet stays localized in space (Figure 2.5c). This is the case if the horizontal length scale of the heterogeneity is larger than the packet dimension.

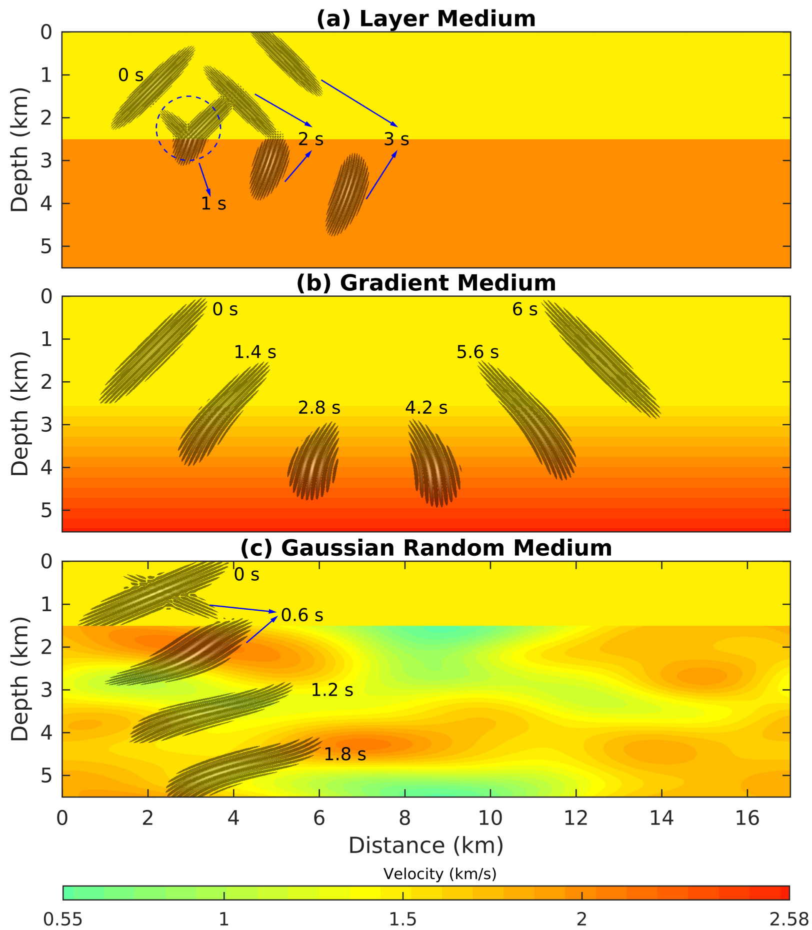

Figure 2.5: GWPs propagating in three heterogeneous media: (a) a layered medium, with a velocity v=1.5 km/s in the top layer and v=2 km/s in the lower layer. (b) a homogeneous medium atop a gradient medium. The homogenous layer has a velocity v=1.5 km/s for depth < 2.5 km. Below the 2.5 km depth, the linearly gradient layer has a velocity gradient dv/dz = 0.36 $/s$. (c) A homogeneous medium (v=1.5 km/s) overlying a Gaussian random medium. The random medium has a scale length $az = 0.2$ km in the vertical direction, and $ax = 5$ km in the horizontal direction. The root-mean-square (RMS) velocity perturbation is 2%. The GWP is propagated in the left part of the top homogenous layer with $p = 64, \gamma = 0.6, \varepsilon = 40$ in (a) and $p = 36, \gamma = 0.6, \varepsilon = 40$ in (b) and (c). For each GWP, snapshots at different times are shown in the model. The snapshot time is labeled adjacent to the GWP.

To summarize the above modeling results in inhomogeneous media, a GWP can retain both its shape and its directional quality during propagation in a variety of media. Thus, it may serve as an excellent substitute for the approximate GBs that were used in Zheng et al. (2013) for fracture characterization.

2.4 Conclusions

We showed how the parameters govern the GWP's properties of localization in space and time during its propagation in the homogeneous model. Furthermore, we propagated the GWPs designed by the same sets of parameters in different velocity media and record the data. The recorded data show that we may need use different sampling rates to avoid artifacts, the GWP propagating with a higher speed needs a higher Nyquist frequency sampaling than the other GWP in our examples.

Then, we studied the propagation of the GWP in heterogeneous media, beyond its original analytical formulation. We found qualitatively that when the packet aspect ratio is small and when there are more oscillations in the packet support along the propagation direction, the GWP will retain its localized shape and directionality over a long propagation distance. In a smooth Gaussian random medium, when the heterogeneity length scale is larger than the size of the packet, the packet moves along the ray path with small distortion. We also observed that when a GWP is incident upon an interface, it splits into a transmitted packet and a reflected packet traveling along the respective ray paths dictated by Snell's law, with both being localized and directional. These properties provide the basis to use GWPs to invert for the subsurface fracture parameters.

3 Construction of 2D Gaussian wave packet data from shot records

3.1 Introduction

Packets or beams are often used as propagators to speed up the algorithms in seismic imaging (Wu et al., 2002). The packets are usually formed from the source side and receiver side separately. However, what would be the recorded data if the source were one packet or beam source is less studied.

Our main goal in this chapter is to generate the GWP wavefield records from point source gathers as if the source were a GWP. Since the GWP provides a local illumination with a specific incident angle on the target, its data record provides us a way to study the medium through the constructed partial wavefield. Based on the analytical formulation of GWP in a homogenous medium provided in Chapter 2, we show a method to construct a GWP source and its corresponding recorded data by using the point sources and shot records. Then, we synthesize the GWP data using point-source wavefield data in two numerical models. Results from numerical examples show that we can get the GWP records as if the source were a GWP source. And we use the constructed data to produce an image of the model with the reverse time migration (RTM) method (Zhou et al., 2018).

3.2 Representation of GWP wavefield from point-source records

Seismic data in the field are acquired/observed in the form of common shot gathers, $D_{obs}(t, \mathbf{x}_g, \mathbf{x}_s)$, where t is the recording time, $\mathbf{x}_g$ denotes the receiver location, and $\mathbf{x}_s$ is the source position. Point sources and receivers are usually located on the same surface A. It is common to assume that the source wavelet in D_{obs} is the Ricker wavelet in field data. Although the exact shape of the wavelet does not matter for our synthesis purpose, we need to keep in mind that real field data are shaped by some source wavelet. The wavefield from a point source interacts with all parts of the velocity model whereas a GWP field interacts with only part of the model. Thus, it would be beneficial to excite a GWP wavefield. However, there is no physical device that can excite a GWP in practice. Therefore, we need to figure out how to synthesize the GWP field using the common shot gathers that are available to us. We will show that such a synthesis can be done with the concept of time reversal (e.g., Zhou, 2014). In the process of synthesizing a GWP wavefield, although the Earth's surface is a free-surface, we will assume there is no free-surface boundary condition. Through four main steps, we are able to simulate a synthesized GWP wavefield from the recorded point-source data.

Step 1 The first step is to design an analytical GWP at time 0 s by Eq. 2.2 in the subsurface at a location $\mathbf{x}_c = (x_0, z_0)$. Since GWP centers around at location $\mathbf{x}_c$ at time 0 s, the location $\mathbf{x}_c$ has to be deep enough such that GWP is entirely in the model. It propagates along a certain direction θ (Figure 3.1a). We can choose a set of desired parameters (p, ε, γ) to obtain the GWP using Eq. 2.2.

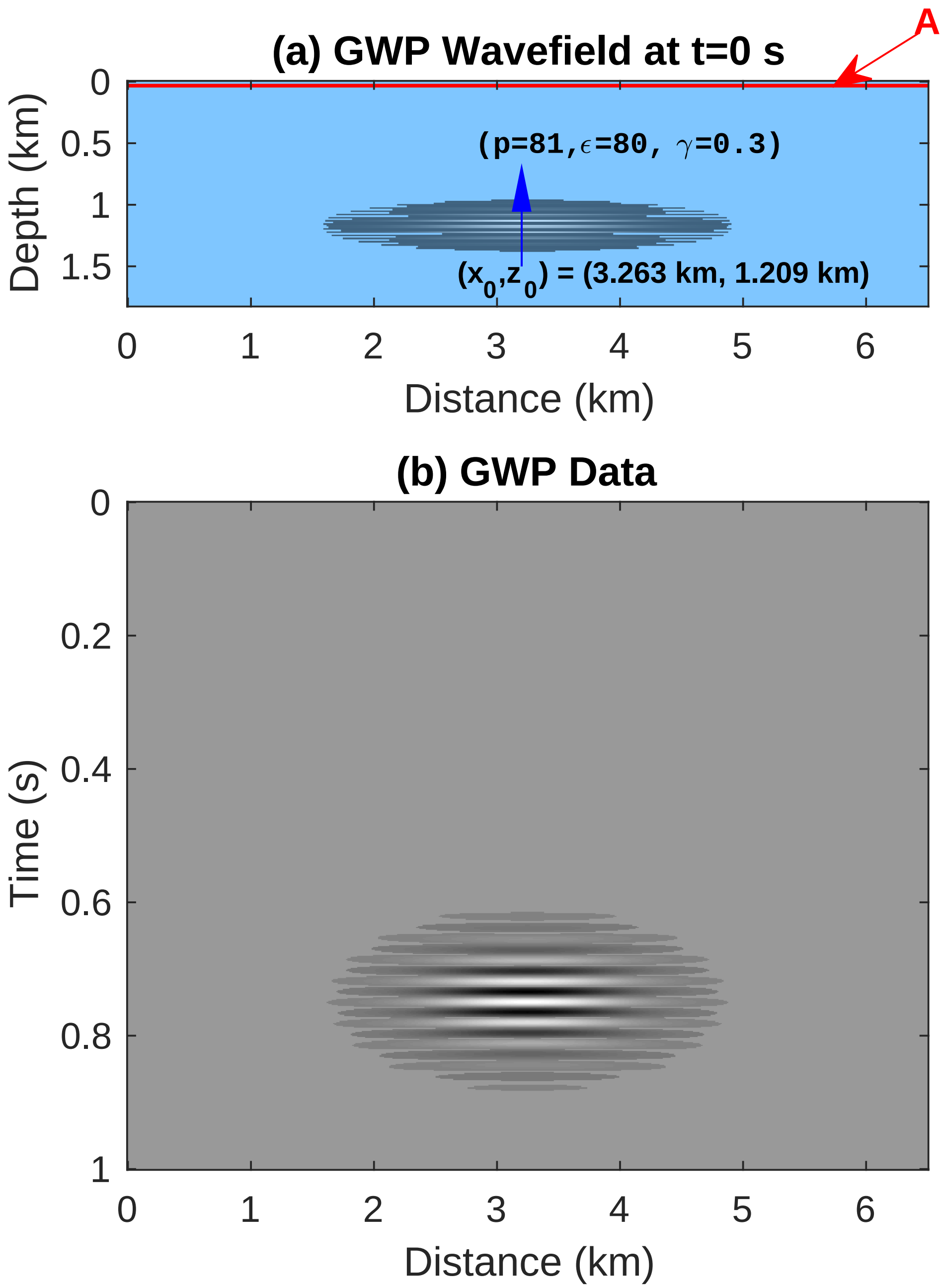

Figure 3.1: Synthesis of a GWP source. (a) The designed GWP overlaid on a constant velocity model (1.5 km/s) at time 0 s, with the propagation angle $\theta = -\pi$ (blue arrow). The center (x_0, z_0) and parameters (p, ε, γ) that define the GWP are shown (black) next to the packet. The red line indicates the surface A where point sources and receivers are located. (b) The recorded GWP data by 501 receivers from 0 to 6.5 km horizontally. The receivers are at depth of 5 m. The receiver interval is a constant (13 m).

Step 2 We propagate the designed GWP along the direction of θ. The GWP moves upward from (x_0, z_0) to the surface A. We record this GWP wavefield $D(t, \mathbf{x}^{'})$ on the surface A with the total recording time length equal to T s, where $\mathbf{x}^{'}$ represents surface locations. We use the local constant velocity near the location (x_0, z_0) to propagate GWP. This near surface velocity can be readily estimated in the field. Hence, we can compute GWP propagation analytically in a constant velocity model (Eq. 2.2). Because GWP is localized in space, the recording $D(t, \mathbf{x}^{'})$ is nonzero only for the partial illuminated region of surface A (Figure 3.1b). The illuminated region depends on the center location $\mathbf{x}_c = (x_0, z_0)$ and propagation direction θ of the designed GWP using desired parameters (p, ε, γ). For those locations that are not illuminated by the packet, the fields are zero.

Step 3 We use the reverse-time concept to propagate the recorded GWP field on surface A downward into the medium. At $\mathbf{x}^{'}$, we time-reverse the recorded $D(t, \mathbf{x}^{'})$ and take it as the virtual GWP source $S_{gwp}(t, \mathbf{x}^{'})$ (Figure 3.2):

$$S_{gwp}(t, \mathbf{x}^{'}) = D(T - t, \mathbf{x}^{'}) \tag{3.1}$$

Step 4 The ideal field data $D_{gwp}^{ideal}(t, \mathbf{x}_g)$ that would be generated by the GWP source is a convolution between the Green's function and the GWP source S_{gwp} :

$$D_{gwp}^{ideal}(t, \mathbf{x}_g) = \int_A G(t, \mathbf{x}_g, \mathbf{x}^{'}) \otimes S_{gwp}(t, \mathbf{x}^{'}) dA(\mathbf{x}^{'}) \tag{3.2}$$

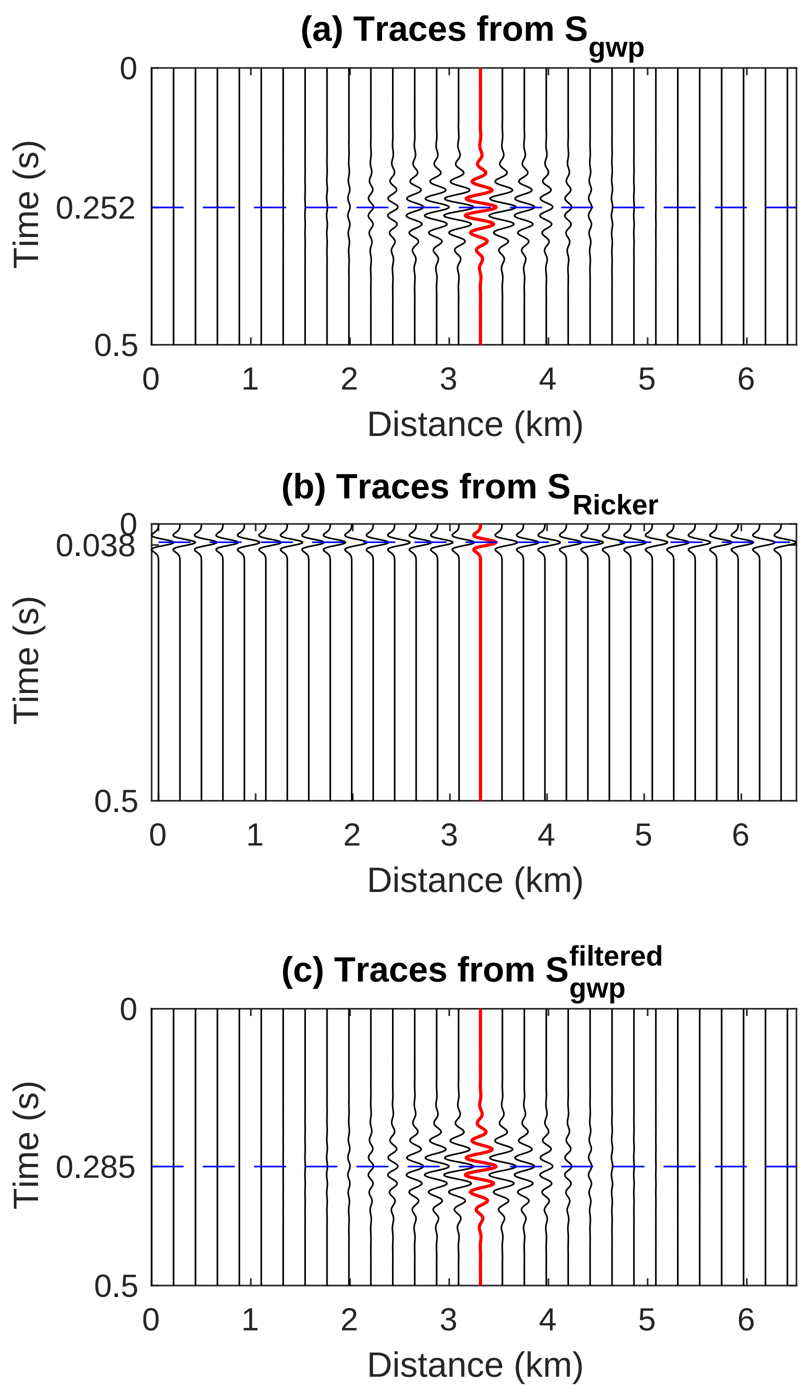

Figure 3.2: Synthesis of a GWP source. (a) The time-reversed GWP data in Fig. 3.1b, which behave as the virtual GWP source S_{gwp}. (b) The Ricker sources S_{Ricker}. (c) The synthesized Ricker-wavelet-shaped GWP source $S_{gwp}^{filtered}$. The red gwp trace in $S_{gwp}^{filtered}$ is obtained by convolution of red trace from S_{gwp} and S_{Ricker} at the same source location (Eq. 3.7). The horizontal blue dashed lines indicate the time arrivals of peak amplitudes in all subplots. Only 30 traces are shown in each subplot, but the total trace number is 501 in each subplot.

in which $G(t, \mathbf{x}_g, \mathbf{x}^{'})$ is Green's function for a point source $\mathbf{x}^{'}$ at with an impulsive source wavelet and a receiver at $\mathbf{x}_g$. The integration is over the recording surface, A. The problem is that we do not know the Greens function for any $\mathbf{x}^{'}$. However, if $\mathbf{x}^{'}$ corresponds to one of the true point-source locations, $\mathbf{x}_s$, this difficulty can be remediated by noting that the recorded point-source trace is again a convolution between Green's function and a source wavelet (e.g., Ricker), e.g.,

$$D_{obs}(t, \mathbf{x}_g, \mathbf{x}_s) = G(t, \mathbf{x}_g, \mathbf{x}_s) \otimes S_{Ricker}(t) \tag{3.3}$$

Therefore, if we assume that the source wavelet is a Delta function $\delta(t, \mathbf{x}_s)$ and constrain ourselves to the true discrete source locations, i.e.,

$$\mathbf{x}^{'} \in \mathbf{x}_s \tag{3.4}$$

Eq. 3.2 can be approximated as

$$D_{gwp}^{approx}(t, \mathbf{x}_g) \approx \sum_{\mathbf{x}_s} G(t, \mathbf{x}_g, \mathbf{x}_s) \otimes S_{gwp}(t, \mathbf{x}_s) dA(\mathbf{x}_s) \tag{3.5}$$

If the source wavelet is a Ricker or already known in Eq. 3.3, we can calculate G by deconvolution of the wavelet from the data. Applying the calculated G to Eq. 3.5, we obtain D_{gwp}^{approx}. However, the deconvolution can be unstable. Instead, we convolve a source wavelet (e.g., Ricker) to both sides of Eq. 3.5 and get

$$D_{gwp}^{syn}(t, \mathbf{x}_g) \approx S_{Ricker}(t) \otimes D_{gwp}^{approx} = \sum_{\mathbf{x}_s} D_{obs}(t, \mathbf{x}_g, \mathbf{x}_s) \otimes S_{gwp}(t, \mathbf{x}_s) dA(\mathbf{x}_s) \tag{3.6}$$

We have completed our synthesis algorithm to obtain D_{gwp}^{syn} using Eq. 3.6. Note that D_{gwp}^{syn} has an extra Ricker wavelet compared to the D_{gwp}^{ideal} data. This is not a significant issue in reality as the Ricker-convolution in Eq. 3.6 can be thought as filtering, which is commonly done in seismic data processing. Eq. 3.6 gives the key step to produce a Ricker-shaped GWP data using recorded shot gathers. In numerical examples where we know the Green's function, the accuracy of D^{syn}_{gwp} can be compared with

$$\begin{aligned} D^{num}_{gwp}(t,\mathbf{x}_g) &= S_{Ricker}(t) \otimes D^{ideal}_{gwp}(t,\mathbf{x}_g) \\ &= S_{Ricker}(t) \otimes S_{gwp}(t,\mathbf{x}_s) \otimes G_{gwp}(t,\mathbf{x}_g,\mathbf{x}_s) \\ &= S^{filtered}_{gwp}(t,\mathbf{x}_s) \otimes G_{gwp}(t,\mathbf{x}_g,\mathbf{x}_s) \end{aligned} \tag{3.7}$$

We notice that the Ricker $S_{Ricker}(t)$ (Fig. 3.2a) filters (or shapes) our $S_{gwp}(t,\mathbf{x}_s)$ to get $S^{filtered}_{gwp}$ (Fig. 3.2c) as a wavelet-shaped GWP source. If we inject this wavelet-shaped GWP source into the model, we will record D^{num}_{gwp}.

We have assumed that the source at every location has the same Ricker wavelet in Eq. 3.6 and the GWP source is calculated in a constant velocity model. However, random noise is unavoidable in field acquisitions (Li et al., 2014) and velocity variations at the source location can cause near-surface statics problems (Zhou 2014). Moreover, we have used summation of shot gathers generated by discrete point sources in Eq. 3.6 to approximate the integration along the surface A (Eq. 3.7). Hence, the source intervals will have an effect on how well the numerical summation can approximate the integration. In the next two parts, we will study these influences of point sources on GWP wavefield propagation, which consequently influences the construction of GWP data, i.e., the approximation in Eq. 3.6.

3.3 Effect of noise and statics

In field seismic data, random noise is common and unpredictable. It often masks our data in seismic imaging and generates unsatisfactory results. Statics problems from the source side may also cause problems by skewing the starting time in the shot gathers to be misaligned at the same time moment.

To see the influence of noise and statics in point source wavelets on our synthesized GWP wavefield, we show three case studies. To produce three different wavelet-shaped GWP sources, we convolve one GWP source with three different point source wavelets. With numerical modeling, we propagate the synthesized $S_{gwp}^{filtered}(t,\mathbf{x}_s)$; into the model gwp to compute the wavefield D_{gwp}^{num}.

Case 1 We consider an ideal situation for Case 1 and will use it to benchmark results in Case 2 and Case 3.

The ideal situation for synthesizing $S_{gwp}^{filtered}(t,\mathbf{x}_s)$ in Eq. 3.7 is to convolve the GWP source with the same Ricker wavelet (Figure 3.3a) at all point source locations. The 501 point sources are located from 0 to 6.5 *km* horizontally. They are at the depth of 1 *m*. The source interval is constant (13 *m*). After convolving this Ricker wavelet with the designed GWP source $S_{gwp}(t,\mathbf{x}_s)$ (Figure 3.3c), we get the Ricker-shaped GWP source and we call it $S_{gwp1}^{filtered}$ (Figure 3.3b). We then propagate it in a two-layered medium using the finite-difference algorithm and record its wavefield at time 2.1 *s*. The wave packet keeps its compact shape and splits into two packets (reflected and transmitted) after interacting with the interface (Figure 3.3c).

Case 2 We show the random noise influences in point source wavelets to the synthesized GWP wavefield by adding Gaussian white noises (Mendel, 1977) to the Ricker wavelets (Figure 3.3d). The SNR in the noise-added Ricker wavelets is equal to 0.01. We convolve the noise-added Ricker wavelets with the GWP source to form the GWP field and we call it $S_{gwp2}^{filtered}$(Figure 3.3e). After propagating it in the same two-layered medium, its wavefield at time 2.1 s shows the reflected and transmitted packets. Additionally, the white noises from $S_{gwp2}^{filtered}$ generate wavefields and mask the compact wave packets (Figure 3.3f) in the medium.

Case 3 We show the statics influences of the point sources by perturbing the Ricker wavelet arrival times at each source location randomly (Figure 3.3g) with the normal distribution ($\mu = 0s, \sigma = 0.003s$) (Silverman, 2018). Compared with time period of the main frequency (30 Hz) in Ricker, the maximum static shift (0.098 s) is more than a quarter of the time period (0.033 s). Correspondingly, the perturbation of Ricker arrival times causes the traces at different locations to be out-of-phase in wavelet-shaped GWP source $S_{gwp3}^{filtered}$(Figure 3.3h). The wavefield at time 2.1 s not only has the reflected and transmitted wave packets, but also contains a smearing wavefield. (Figure 3.3i). The smearing wavefield, in this case, is due to the interference among the out-of-phase traces in $S_{gwp3}^{filtered}$.

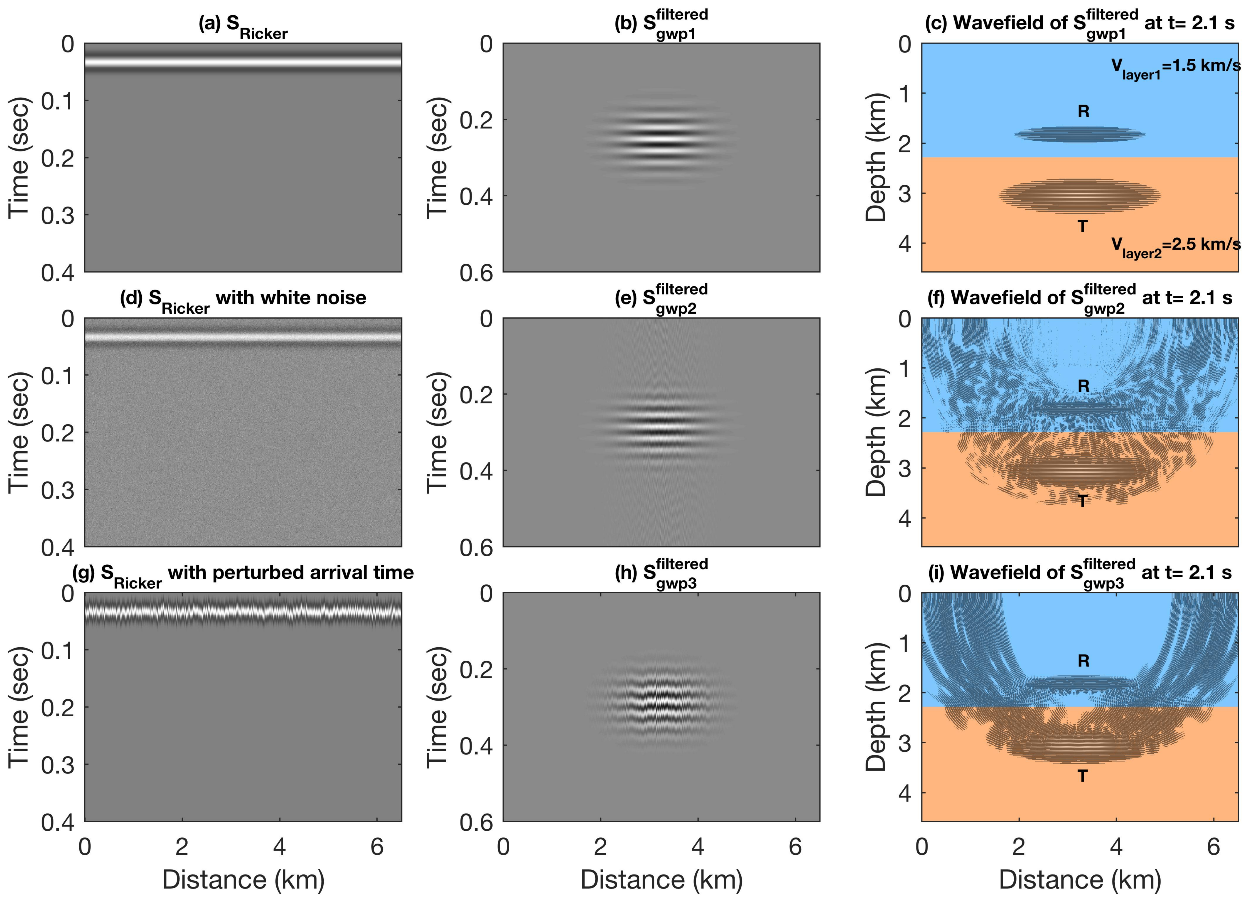

Figure 3.3: Effects of point-source wavelets on the propagation of the wavelet-shaped GWP source: (a) point sources with the same Ricker wavelet. (b) $S_{gwp1}^{filtered}(p = 81; \varepsilon = 80; \gamma = 0.3)$ synthesized by convolution of S_{gwp} (Fig. 3.2a) with S_{Ricker} in (a). (c) The wavefield at t = 2.1 s due to $S_{gwp1}^{filtered}$ (d) S_{Ricker} in (a) with white noise added. (e) $S_{gwp2}^{filtered}$ synthesized with noise-added S_{Ricker} in (c). (f) The wavefield at t = 2.1 s due to $S_{gwp2}^{filtered}$. (g) S_{Ricker} in (a) with arrival time perturbed randomly. (h) $S_{gwp3}^{filtered}$ synthesized with starting-time-perturbed S_{Ricker} in (g). (i) The wavefield at t = 2.1 s due to $S_{gwp3}^{filtered}$. All snapshots are overlaid on the two-layered medium with velocities 1.5 km/s and 2.5 km/s. R indicates the reflection from the horizontal interface, and T indicates the transmitted wavefield.

3.4 Effect of point-source interval

In Eq. 3.6, we perform the summation of discrete shot gathers on the surface A to construct the GWP data. Thus, the point-source interval is crucial to approximate well the integration by summation of shot gathers. To study the effect of the discrete source interval on the GWP wavefield numerically, we generate wavelet-shaped GWP sources with four different point source intervals based on Eq. 3.7. We propagate each wavelet-shaped GWP source into the same velocity model and produce a snapshot of the wavefield at time 2.1 s correspondingly.

In the previous $S_{gwp1}^{filtered}$ $(p = 81, \varepsilon = 80, \gamma = 0.3)$ (Figure 3.3b), the point sources have a constant interval of 13 m. The snapshot (Figure 3.3c) at t = 2.1 s shows the GWP wavefields propagate as compacted packets without artifacts. We then directly extract traces from $S_{gwp1}^{filtered}$ with four different source intervals (26 m, 36 m, 52 m, 65 m). Propagating the 4 new-sampled wavelet-shaped GWP sources, we will record their wavefields to see if any artifacts generate.

To give a quantitative description of the GWP wavefields from the four source-interval resampled $S_{gwp1}^{filtered}$s. We compare their source intervals with the main wavelength of this Ricker-shaped GWP packet. The main wavelength is 50 m in the first layer. When the source interval (26 m) is approximate to half (25 m) of the main wavelength, this wavelet-shaped GWP source propagates with compact packet field (Figure 3.4a). For source intervals which are 39 m, 52 m, and 65 m, the wavelet-shaped GWP sources do not achieve complete destructive interference to have compact "GWP packet" wavefields only. Artifacts (Figure 3.4 b-d) are generated due to insufficient spatial sampling of the wavelet-shaped GWP source. These artifacts will appear in our constructed GWP data if the discrete point sources have sparse intervals.

We conclude that the receivers may not only record Ricker-shaped GWP wavefield, but also the artifacts generated due to noise, random starting time in point sources, and sparse source interval. In our investigations, the Gaussian noise (SNR equals to 0.01) and the random time-arrival shift with a normal distribution ($\mu = 0s, \sigma = 0.003s$) in the Ricker wavelets, can cause the Ricker-shaped GWP source $S_{gwp1}^{filtered}$ ($p = 81, \varepsilon = 80, \gamma = 0.3$) generate obvious artifacts. In the resampled $S_{gwp1}^{filtered}$ (propagation direction 0^o), artifacts generate when the source interval is larger than 3/5 main wavelength in the first layer. Before doing the synthesis of GWP records, practical preprocessing (e.g., static correction and noise suppression) to shot records (Wang, 2006; Zhang et al., 2014) may be necessary.

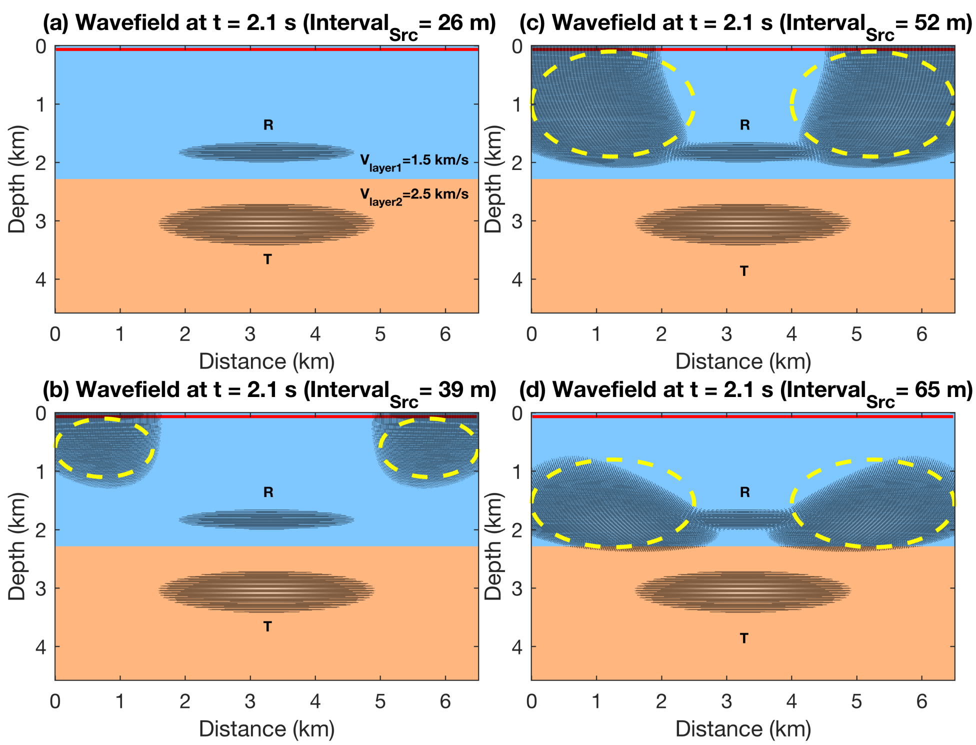

Figure 3.4: Four wavefields at t = 2.1 s in the two-layered velocity medium, due to the GWP source with four different source intervals. (a) Source interval is 26 m. (b) Source interval is 39 m. (c) Source interval is 52 m. (c) Source interval is 65 m. The red line indicates the source locations in each plot. The yellow dashed line circles the artifacts out.

3.5 Numerical examples

Following the procedures in the previous section, we show two numerical examples on the construction of GWP data record from shot records. Moreover, we show its application in the seismic imaging and illumination analysis with the second model.

In our first numerical example, we make a two-layered model (Figure 3.5a). There is a circular-shaped low-velocity anomaly with a radius of 0.25 *km* centered at (x_c= 2.26 *km*, z_c = 0.3 *km*) in the first layer. The source is located at a depth of 5 *m*, starting from a horizontal position 275 *m* to 1825 *m* at an interval of 5 *m*. The receivers are at the depth of 5 *m* and range across the whole model with the interval of 5 *m*. The source wavelet is a Ricker with center frequency 30 *Hz*. With a shot record, we show that the data not only have the reflection from the interface, but also the diffractions caused by the velocity anomaly (Figure 3.5b).

To get the synthesized GWP data using point-source wavefields, we record our designed GWP as $D(t,\mathbf{x}_g^{gwp})$ at receivers that are collocated with point sources. We time-reverse this GWP data to form a GWP source $S_{gwp}(t,\mathbf{x}_s)$ (Figure 3.5c). Using the operation expressed by Eq. 3.6, we produce the synthesized GWP data $D^s_{gwp}(t,\mathbf{x}_g)$ from the point source records (Figure 3.5d).

To verify our synthesized GWP data is the same as the modeled GWP wavefield, we need to form the GWP source $S^{syn}_{gwp}(t,\mathbf{x}_s^{gwp})$ with Eq. 3.7 and propagate it into the model. We denote the recorded the GWP wavefield at receivers by $D^d_{gwp}(t,\mathbf{x}_g)$ (Figure 3.5e). After comparison with their amplitudes, we find that the direct record of GWP source and the synthesized GWP data are indeed the same, apart from the slight differences due to numerical precision (Figure 3.5f).

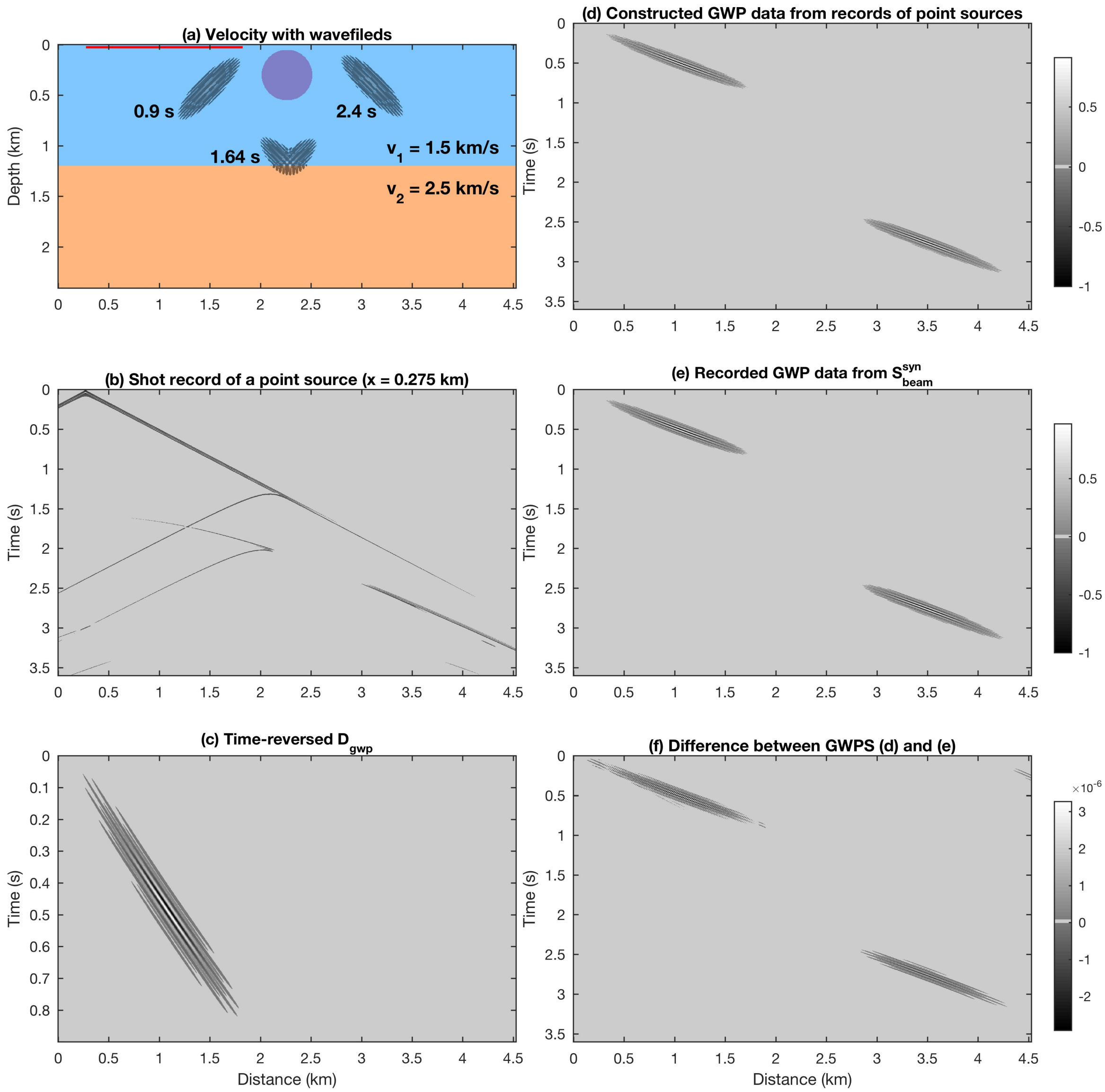

Figure 3.5: GWP data construction from point source records. (a) A two-layered medium with a low velocity (0.1 km/s) zone in the upper layer. Three wavefield snapshots of a filtered GWP source (locations indicated by the red line) are shown. (b) Data record from a Ricker source located at 0.275 km. (c) The time-reversed GWP data used for building the filtered GWP source. (d) GWP data synthesized from point source records. (e) GWP data directed recorded from the filtered GWP source. (f) Wavefield difference between (d) and (e).

Furthermore, we show the snapshots of the filtered GWP source at three discrete time moments (Figure 3.5a). During the propagation, this GWP source does not interact with the low-velocity anomaly from this specific initial propagation direction. By constructing such GWP data, we can study the wavefield interacted with the specific part of the model.

In the second numerical model, we show an application of GWP in the seismic imaging. In the two-layered model, a triangle-shaped low-velocity anomaly is present in the first layer (Figure 3.6a). We generate a GWP source to image the targeted area of the model. The point shot data obtained in this model show strong scattered wavefields besides the direct arrivals and the interface reflection (Figure 3.6d). But with our GWP source and its corresponding constructed GWP data (Figure 3.6e & f), we can extract exclusively the multiple. This extracted GWP multiple follows the ray geometry (Figure 3.6b) and bounces between the layer interface and the triangle base. We propagate this GWP source and the time-reversed GWP data in the model to form an image using the RTM (Liu et al., 2016). In the image, we see this GWP only imaged three local parts indicated by the green boxes (Figure 3.6b). The horizontal resolution is controlled by the GWP width, and the vertical resolution is restricted by the narrow frequency band in the GWP source. With the seismic illumination analysis (Geng et al., 2012), the GWP source only illuminates the area along its propagation path (Figure 3.6c). This is a feasible way to control the seismic illumination in the model through the data set. Though we only use one GWP with a specific propagation angle to construct GWP data and do the seismic imaging, it is doable to design GWPs at different locations and with different propagation angles. With the specific chosen GWP and construct GWP data, we are able to image the medium in the sense of locality.

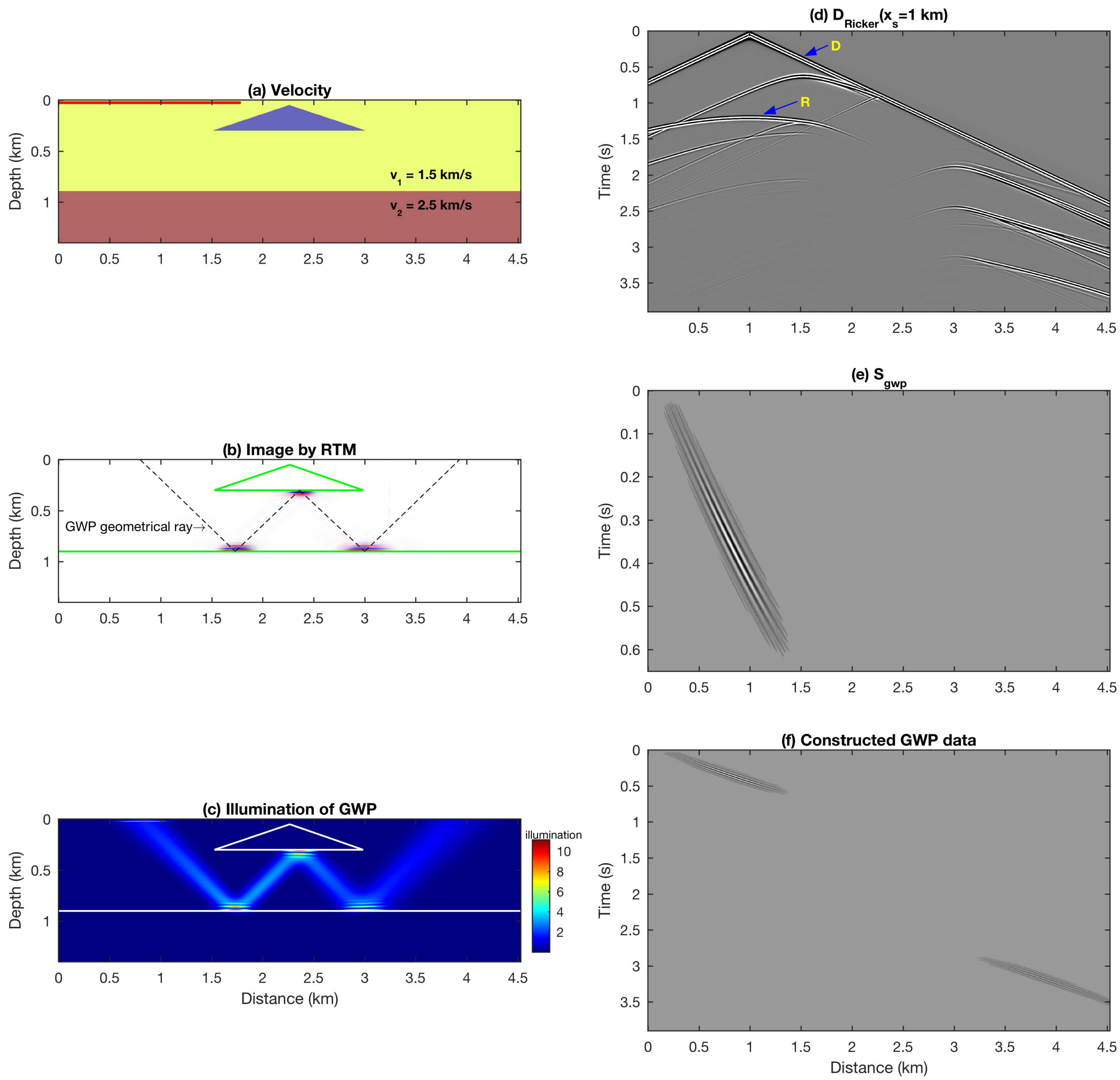

Figure 3.6: GWP data construction and the partial RTM image from the constructed GWP data. (a) A two-layered medium with a low velocity (0.1 km/s) zone in the upper layer. The red line indicates the source locations at depth of 5 m. (b) The RTM image from GWP wavefield. The green boxes show the imaged area. The red dash line shows the central ray geometry of the extracted multiple. (c) The illumination of the GWP source. (d) Data record from a Ricker source with D and R indicating the direct arrival and the reflection from the interface. The rest of wavefields are due to the anomaly. (e) The GWP source. (f) GWP data constructed from point source records as if the source were a GWP source at the red line segment in (a). The green lines in (b) and white lines in (c) denote the anomaly shape and the interface in (a).

3.6 Discussion

Since the synthesized GWP wavefield behaves as a local plane wave, we can design it to interact with a target area with many different propagation angles. We showed its ability in seismic imaging to image local areas. GWP can also be useful in fracture characterizations (Hu and Zheng, 2018a). With the constructed GWP dataset, we could study some specific property (e.g., fractures) of the medium, which is more difficult to study if we process the seismic data of point sources based on the conventional processing flow.

Another potential application of GWP is to interpolate the seismic data set. Because real data may have missing traces, curvelets and dreamlets have been used for the seismic data interpolation (Herrmann and Hennenfent, 2008; Wang et al., 2014). Moreover, seismic data interpolation is the key part for applying compressive sensing in the seismic acquisition. Thus, we may see more different packets (e.g., GWP) to be invented and applied to the seismic data interpolation.

3.7 Conclusions

In this chapter, we demonstrated the process to construct a GWP dataset in the time domain from shot records. We investigated the point sources' influences on the GWP source propagation. Based on the propagation of a proper GWP source, we found that the GWP packet propagates towards a definite direction without diffraction, which is different from the wavefield generated from a point source. With the numerical examples of synthesizing the GWP wavefield in the data domain, we created the wavefield propagating along a certain ray path and avoiding interactions with areas away from such a path. With the RTM applied to the GWP dataset, we produced a partial image of the model.

4 Fracture characterization with 2D Gaussian wave packet

4.1 Introduction

Knowing the distributions of subsurface fractures is crucial to Earth sciences and related fields (e.g., Le Pichon and Fox, 1971; Olsson et al., 1992; Hall et al., 2003). This can impact many applications that include hydraulic fracturing, nuclear waste storage, exploitation of geothermal energy, and probing the stress state. Since most geolocical structures made by interfaces are sub-horizontal, conventional structural seismic imaging has been very effective in delineating these structures. However, fractures are usually alined vertically in the subsuface with large angles, and such a geometry pattern makes conventional seismic imaging of limited use in portraying vertical fractures.

For fractures with a preferred orientation, many authors (e.g., Thomsen, 1995; Liu et al., 2000) have shown that the host rock can be treated as an effective anisotropic medium (the effective medium theory or EMT). Rüger (1998) and Lynn and Thomsen (1990) demonstrated that the P-wave and S-wave reflection coefficient should depend on azimuth (AVAZ). In addition, elastic anisotropy can split an incident shear wave into a fast shear wave and a slow shear wave (Crampin, 1985)(Crampin, 1985). In traditional seismic processing, the AVAZ and the shear-wave splitting are the main tools for remote detection of subsurface fractures.

Besides the anisotropy-based methods, scattering approaches were also proposed. The fracture transfer function (FTF) and the scattering index (SI) method (Willis et al. 2006; Fang et al. 2013,

2014) were developed to invert for fracture orientation. These methods exploit the differences between waves traveling along fracture corridors and those propagating perpendicular to fracture planes. The diffraction imaging uses singly scattered waves by fractures (non-specular reflection of fractures, Fomel et al. 2007) to identify subsurface fractures. Both the effective medium approach and these scattering-based approaches have challenges in distinguishing and resolving multiple sets of fractures.

Zheng et al. (2013) developed a new approach to use multiply scattered waves spawned by a local set of fractures illuminated by a local plane wave. The propagation direction and amplitude of the scattered wave can be used to estimate various fracture parameters, including the density, orientation and compliance of fractures. They showed that their method could invert for spatially dependent fracture parameters for coexistent multiple fracture sets. However, both the incident and scattered waves need to be localized in space and be directional. In their paper, the local plane wave is created by a focusing Gaussian beam (GB) shot from the surface (Červenỳ et al., 1982; da Costa et al., 1989; Hill, 1990). It is well known that the GB will lose its directionality over a long propagation distance and the beam width tends to diverge as well (Ralston, 1982; Babich and Ulin, 1984; Hill, 2001). We need a better wave object, which can remain localized and directional after long distance. To minimize such diffraction of the global GB, Chen et al. (2006) suggested re-decomposing the wavefield into local Gabor-Daubechies beamlets at each step in its downward continuation. To implement this propagation, we need to have an accurate velocity model that is unavailable in general.

In this chapter, we begin with a brief review of fracture characterization using the plane-wave multiple scattering theory. The basic idea is that when a plane wave is incident upon a group of fractures, the scattered waves contain information of the fracture parameters: fracture orientation, density, and compliance. To obtain spatially dependent fracture properties, we use the localized GWP as a local incident plane wave. The algorithm is target oriented. To test the feasibility of our algorithm, we conduct three synthetic tests. All examples are conducted in 2D space so that the orientation of the fractures is fixed. We only need to invert for the fracture spacing as a function of space.

4.2 Brief review of plane wave scattering

For a plane wave interacting with a set of discrete, periodic, and parallel vertical fractures, the scattering direction and the incident direction are related (Zheng et al., 2013):

$$\mathbf{K}_T^g(n) = \mathbf{K}_T^s(n) + n\frac{2\pi}{a}\hat{\phi} \tag{4.1}$$

where the incident-wave wavenumber $\mathbf{K}^s = (\mathbf{K}_T^s, K_Z^s)$ has two components (horizontal $\mathbf{K}_T^s$ and vertical K_Z^s); similarly $\mathbf{K}^g = (\mathbf{K}_T^g, K_Z^g)$ is the wavenumber for the scattered plane wave to receivers; $\mathbf{K}_T^g = \omega \mathbf{p}_g$ where $\mathbf{p}_g$ is the transverse component of the scattered-wave slowness vector; $\hat{\phi}$, the fracture orientation, is defined as the unit vector perpendicular to the fracture plane; a is the spacing between neighboring fractures. It is apparent that the wave can scatter into different directions designated by n (Figure 4.1). Each propagation direction, n, includes both singly and multiply scattered waves. Though n can be any integer, we use $n = -1$ to detect fracture properties. The main reason is that, if n is too large, the resultant vertical wavenumber $|n|$ may become purely imaginary, making the scattered waves evanescent. We note that $n = 0$ corresponds to the specular reflection commonly used in fracture inversion using reflected-wave amplitude information.

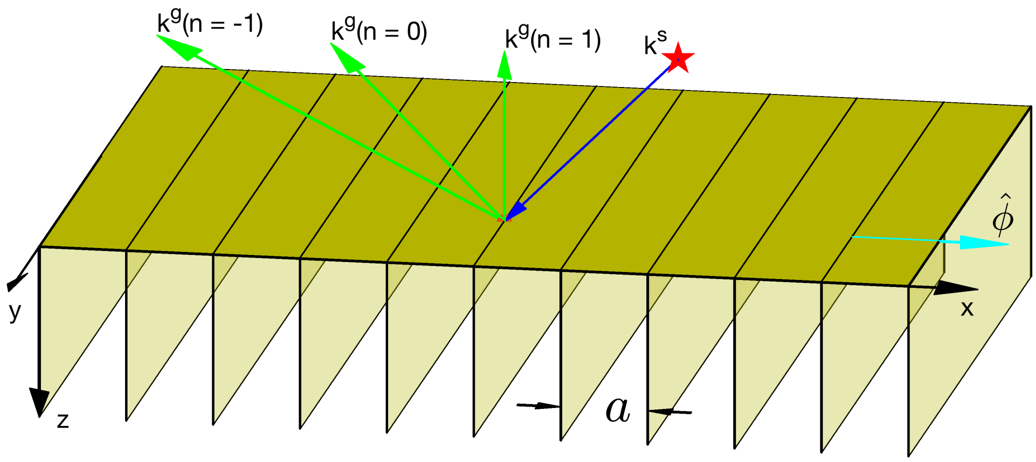

Figure 4.1: Schematic plane wave scattering caused by equally spaced vertical fractures underground.

Eq. 4.1 should work in both acoustic and elastic media. In an elastic medium, the scattering wave will generally be partitioned into P and S waves due to a pure incident P or S wave. It is possible for us to utilize different incident-scatttering wave pairs (P-P, P-S, S-P, S-S) to characterize fractures.

Eq. 4.1 describes the kinematics of plane-wave multiple scattering produced by an infinite number of periodic fractures. However, the fracture network with a single constant spacing is too ideal for the real world. Fracture spacings and orientations may vary due to the changing of local stresses, local rock properites, etc. To make the scattering theory explained by Eq. 4.1 still work in such a situation, we employ the GWP as a local plane wave to interact with fractures locally. In such a way, the GWP can characterize a fracture network having the variation of fracture spacing and orientations. Examplified by Zheng et al. (2013), two coexisting orthoganal fracuture networks in which fracture spacing varies spacially can be characterized successfully by local Gasussian beams. In Hu et al. (2018), the random spacing fractures were characterized by the local GBs developed in Zheng et al. (2013).

In the following synthetic tests, we apply this theory locally for 2D acoustic cases. We confine ourselves to characterize the 2D vertical fractures in a horizontal layer. When the fractured layer is dipping, the coordinate transformation can be applied at the locations of fractured layer to cahracterize fractures properly using Eq. 4.1 (Hu and Zheng, 2018b).

4.3 Methodology of fracture characterization

The GWP fracture characterization algorithm is target-oriented and frequency dependent. The inputs to the algorithm include: (1) a velocity model for tracing the rays of the scattered waves, (2) the approximate depth of fractured reservoir and (3) recorded shot gathers.

The first step is to select a subsurface fracture target location $\mathbf{r}$ in the model. We then shoot a GWP from a location $\mathbf{r}_0$ at surface toward the fracture target. We can obtain the GWP gather $D_{gwp}^{syn}(t, \mathbf{x}_g)$ using the three-step synthesis approach (Eq. 3.6). Since we have a velocity model, we can calculate $\mathbf{K}^s$ using ray tracing from the shooting location to the target. With $n = -1$, we grid-search fracture spacing and orientation $(a, \hat{\phi})$ to calculate $\mathbf{K}^g$ at $\mathbf{r}$ to trace the scattered ray back to the surface location $\mathbf{x}_g^e$. For a pair of $(a, \hat{\phi})$, we can compute the total traveltime $t_{arrival}$ from the GWP shooting point to the target then to the receiver. Due to localization of the GWP in time and in space, we window $D_{gwp}^{syn}(t, \mathbf{x}_g)$ around $t = t_{arrival}$ and around $\mathbf{x}_g = \mathbf{x}_g^e$:

$$D_{gwp}^{win}(t, \mathbf{x}_g | \omega, \theta) = g_t(t - t_{arrival}) g_x(\mathbf{x}_g - \mathbf{x}_g^e) D_{gwp}^{syn}(t, \mathbf{x}_g) \tag{4.2}$$

where g_t can be Gaussian windowing function and g_x be a box car function. In the 2D case, we can use the scalar θ to replace the vector $\hat{\theta}$. The true fracture parameter a should yield a $\mathbf{K}^g$ which matches the wavefield direction information in $D^{win}_{gwp}(t,\mathbf{x}_g|\omega,\theta)$ generated by an incident GWP with progagation θ. We probe this consistency using slant stacking for every frequency ω in the data.

In this windowed data, we first implement a slant stack with a slowness vector $\mathbf{p}_g$ as $A_{sacttered}$:

$$A_{sacttered}(\mathbf{p}_g,\tau|\omega,\theta) = \int_A D^{win}_{gwp}(\tau+\mathbf{p}_g\cdot\mathbf{x}_g,\mathbf{x}_g|\omega,\theta)d\mathbf{x}_g \tag{4.3}$$

where τ is the intercept time. We then define the scattered energy $E_{sacttered}$ by the integration of the absolute $|A_{sacttered}|$:

$$E_{sacttered}(\mathbf{p}_g,\omega,\theta) = \int_0^\infty |A_{sacttered}|d\tau \tag{4.4}$$

The maximum value of $E_{sacttered}$ should occur at $\mathbf{p}_g$ corresponding to the true fracture spacing a (Eq. 4.1). We are dealing the 2D space now so we ignore the fracture orientation $\hat{\phi}$. We can repeat this processing for other frequencies ω too. However, they should produce the same a. In order to combine results from different frequencies ω_I and different GWP incident angles θ_J, we multiply all the $E_{sacttered}$'s to build a new function $E^{gwp}_{sacttered}$ that varies only with $\mathbf{p}_g$:

$$E^{gwp}_{sacttered}(\mathbf{p}_g) = \prod_{I=1}^{N}\prod_{I=1}^{M} E_{sacttered}(\mathbf{p}_g,\omega,\theta) \tag{4.5}$$

where I, J are the indexes of the selected discrete frequencies and propagation angles, respectively, and N, M are the total numbers of the discrete ω, θ, respectively. We do not use simple linear summation type stacking in Eq. 4.5 here since we want to emphasize the consistency of $\mathbf{p}_g$ across a wide frequency range and among all different incident angles. Since $\mathbf{p}_g$ and a are one-to-one according to Eq. 4.1, we can rewrite $E^{gwp}_{sacttered}(\mathbf{p}_g)$ as $E^{gwp}_{sacttered}(a)$. Therefore, the trial spacing a resulting in the maximum of $E^{gwp}_{sacttered}(a)$ will be considered as the final inverted spacing for the subsurface fractures.

The use of the velocity model in our algorithm is to find the scattered wavenumber and approximate time window. The velocity model here does not have to be very accurate, in contrast to the case for seismic migration.

To illustrate the method described above, we use a GWP ($p = 144, \gamma = 0.5, \varepsilon = 80$) with 5 different incident angles ($0^o, 15^o, 30^o, 45^o, 60^o$) to interact with one set of fractures embedded in a constant velocity model($2.1km/s$) (Figures 4.2 to 4.6). With the recorded data from each GWP with a specific incident angle, we scan the data with the different trial spacing at each selected frequency as in Eq. 4.4 (Figure 4.7). To get a final result as the fracture spacing, we multiply the data along the frequency and trial spacing as in Eq. 4.5 (Figure 4.8). We find that the multiple scattering directions is more obvious when the incident angle is large (Figure 4.6). This is due to the incident wave having a larger horizontal wavenumber correpondingly.

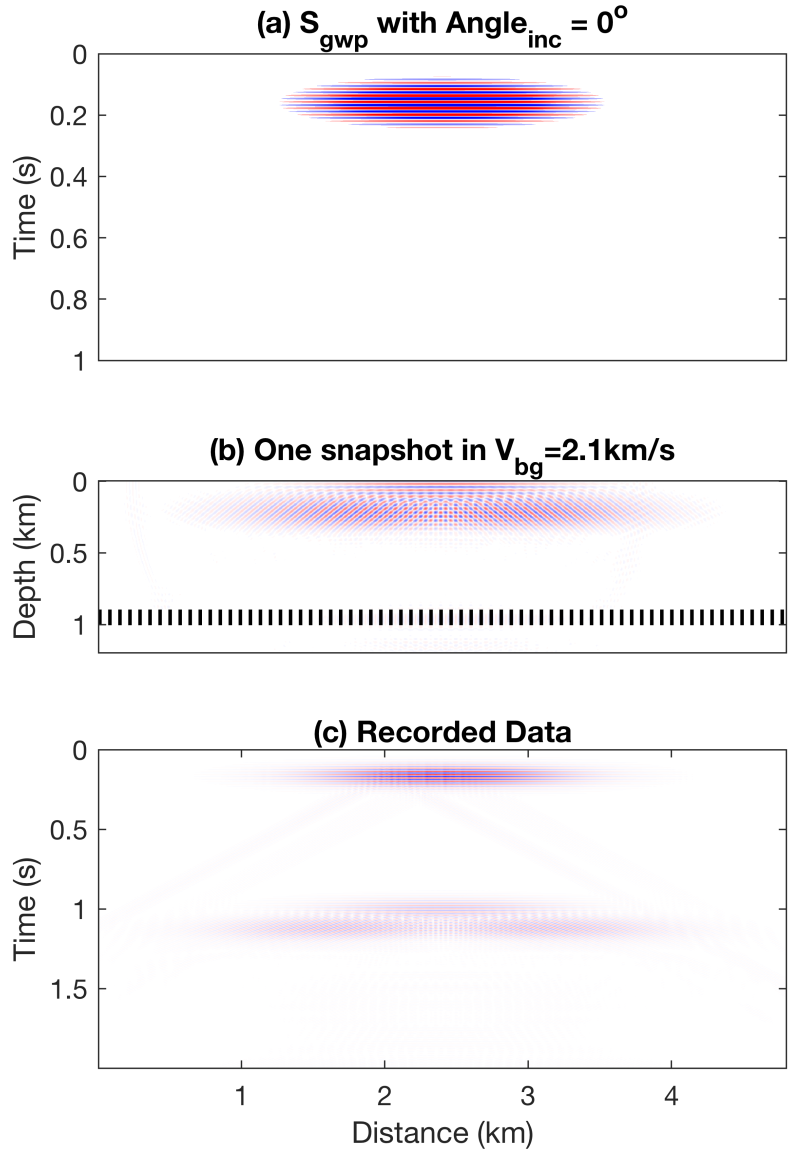

Figure 4.2: (a) GWP with the incindent angle 0^o. (b) Its corresponding snapshot, the black line segments indicate the fractures. (c) The GWP data recorded at the surface.

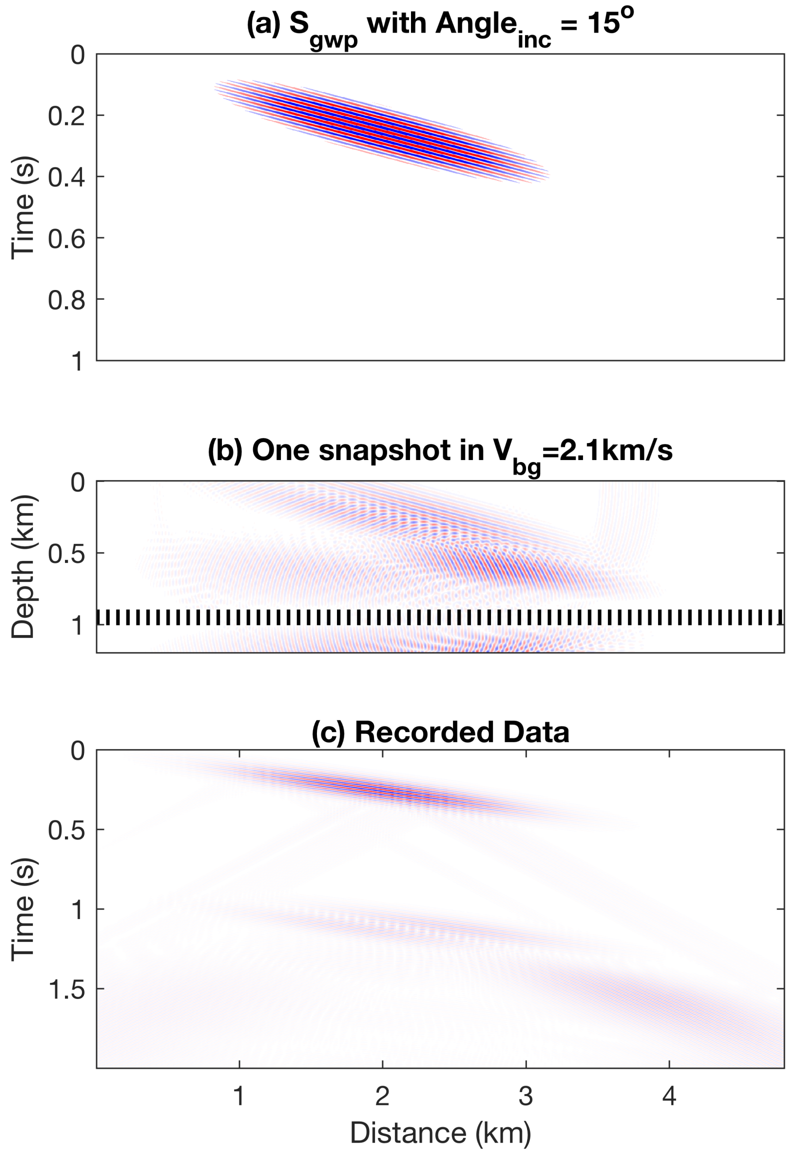

Figure 4.3: (a) GWP with the incindent angle 15^o. (b) Its corresponding snapshot, the black line segments indicate the fractures. (c) The GWP data recorded at the surface.

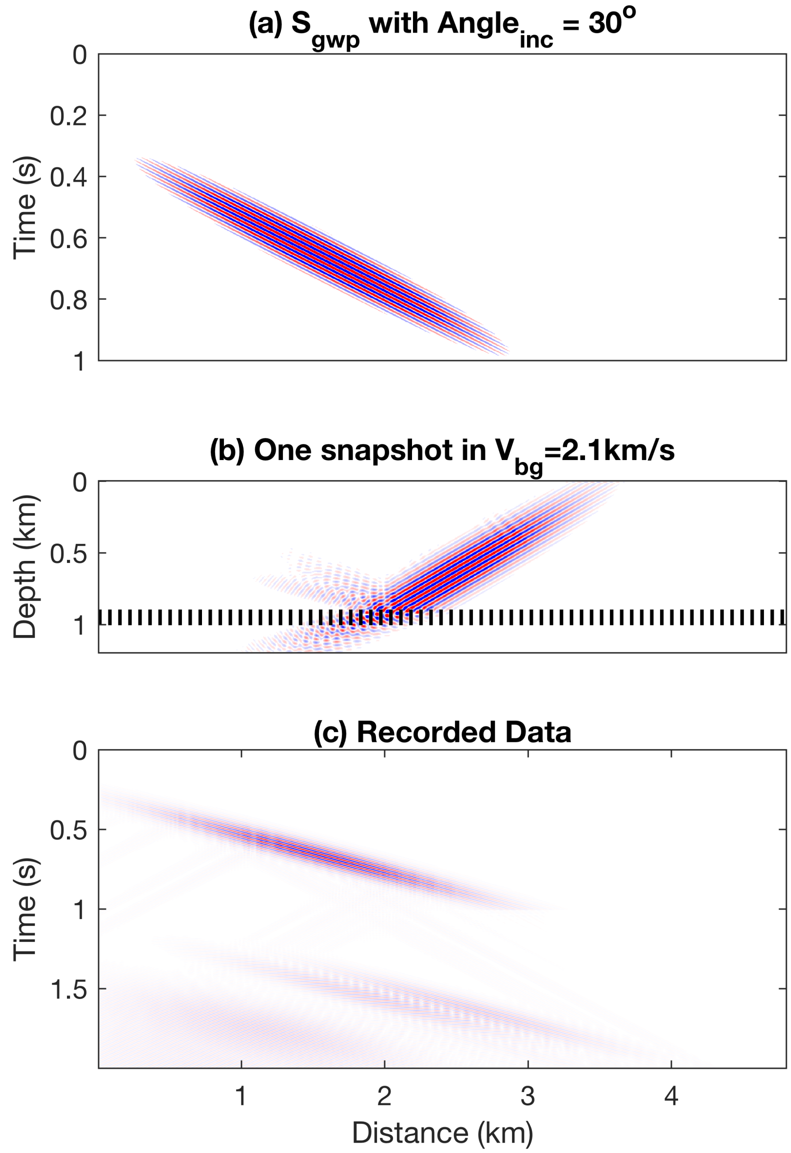

Figure 4.4: (a) GWP with the incindent angle 30^o. (b) Its corresponding snapshot, the black line segments indicate the fractures. (c) The GWP data recorded at the surface.

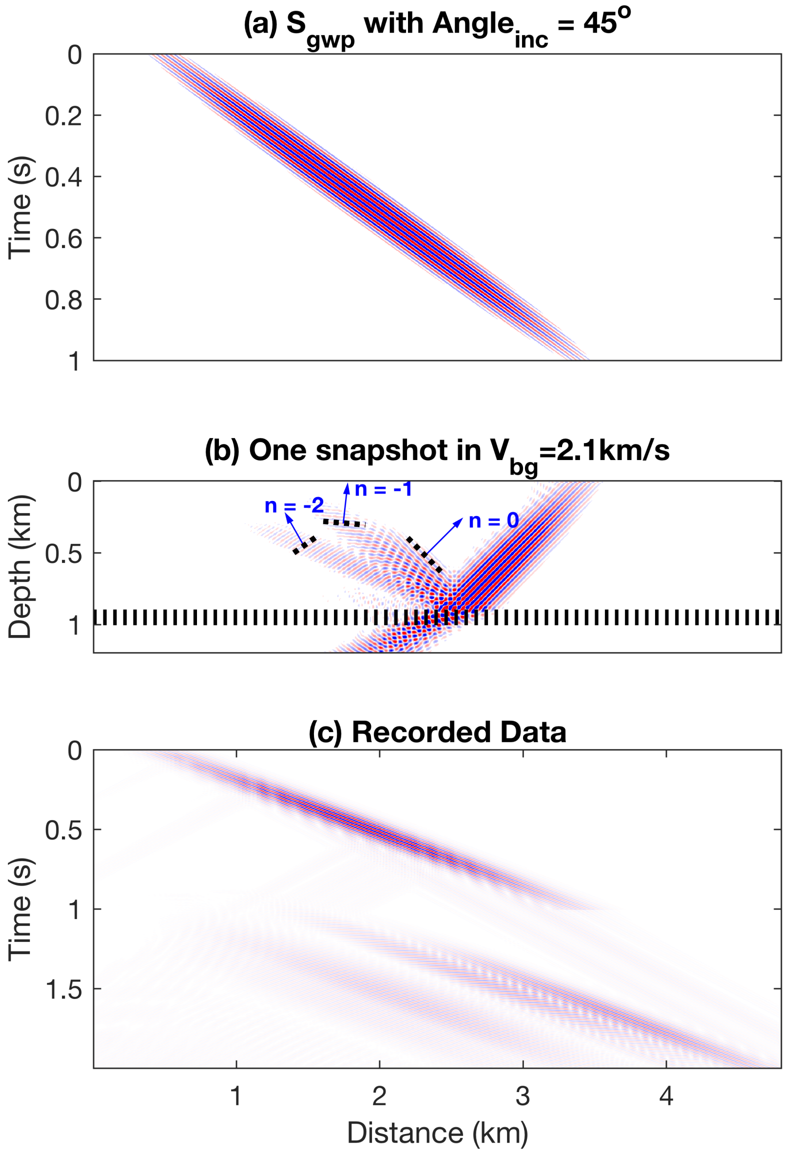

Figure 4.5: (a) GWP with the incindent angle 45^o. (b) Its corresponding snapshot, the black line segments indicate the fractures. (c) The GWP data recorded at the surface. The blue arrows indicate the scattering directions and the dashed line segments indicate the corresponding local plane wavefronts in (b).

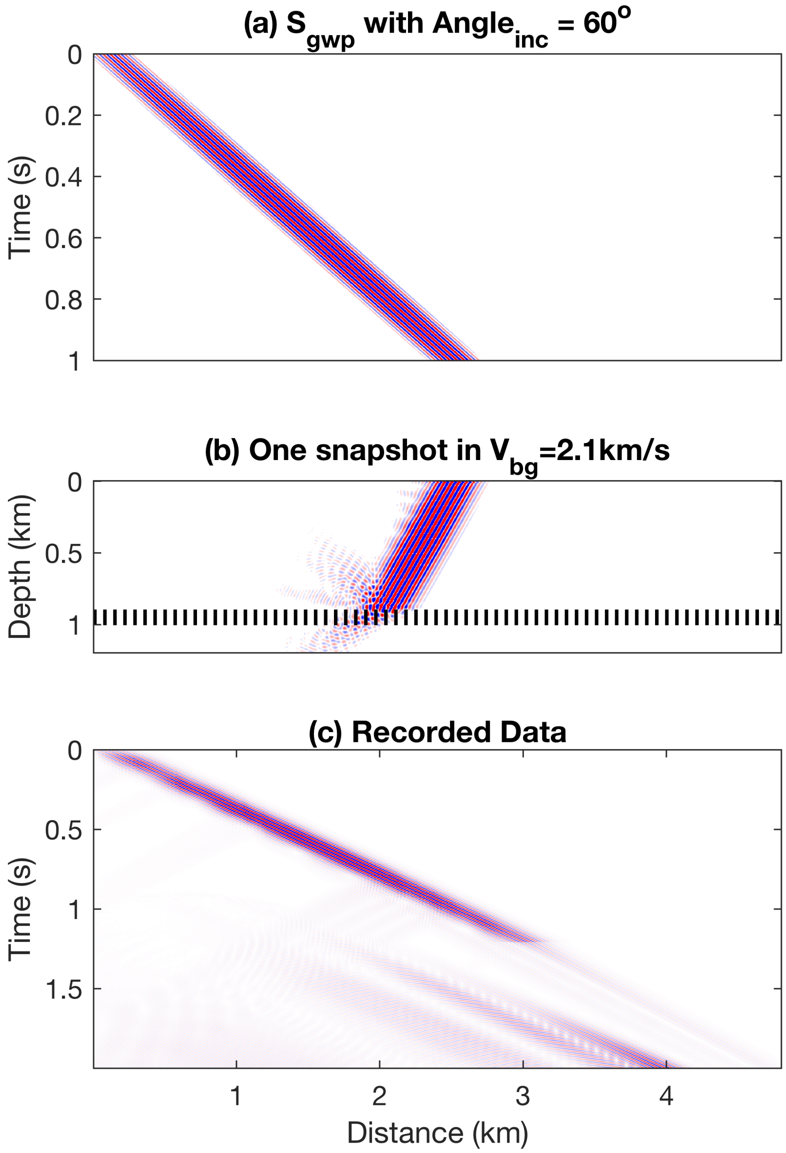

Figure 4.6: (a) GWP with the incindent angle 60^o. (b) Its corresponding snapshot, the black line segments indicate the fractures. (c) The GWP data recorded at the surface.

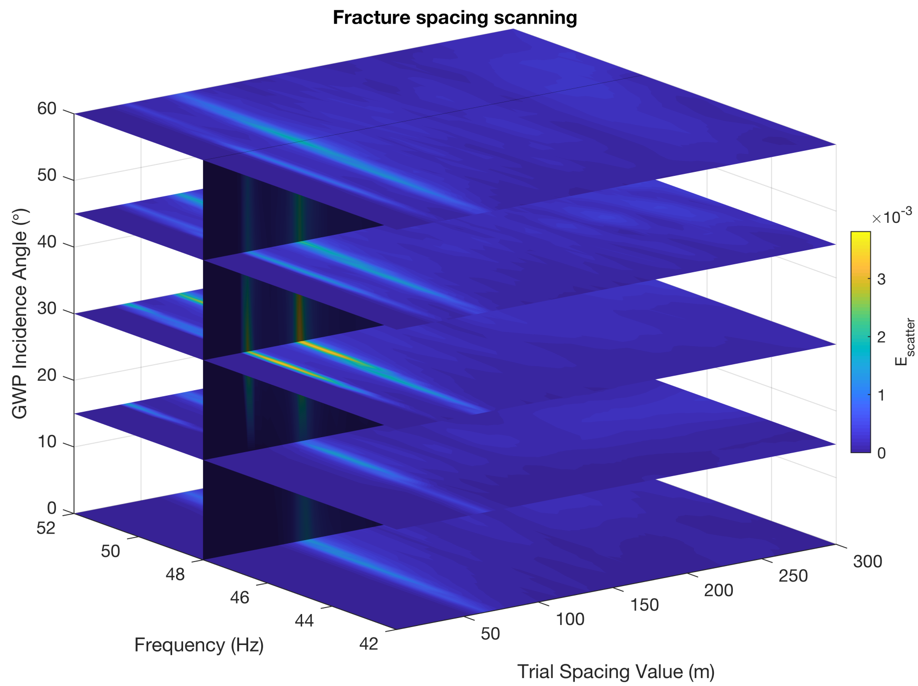

Figure 4.7: $E_{sacttered}(\mathbf{p}_g, \omega, \theta)$ with repsect to the incident angle θ, frequency ω and Trial spacing values which correspond to $\mathbf{p}_g$.

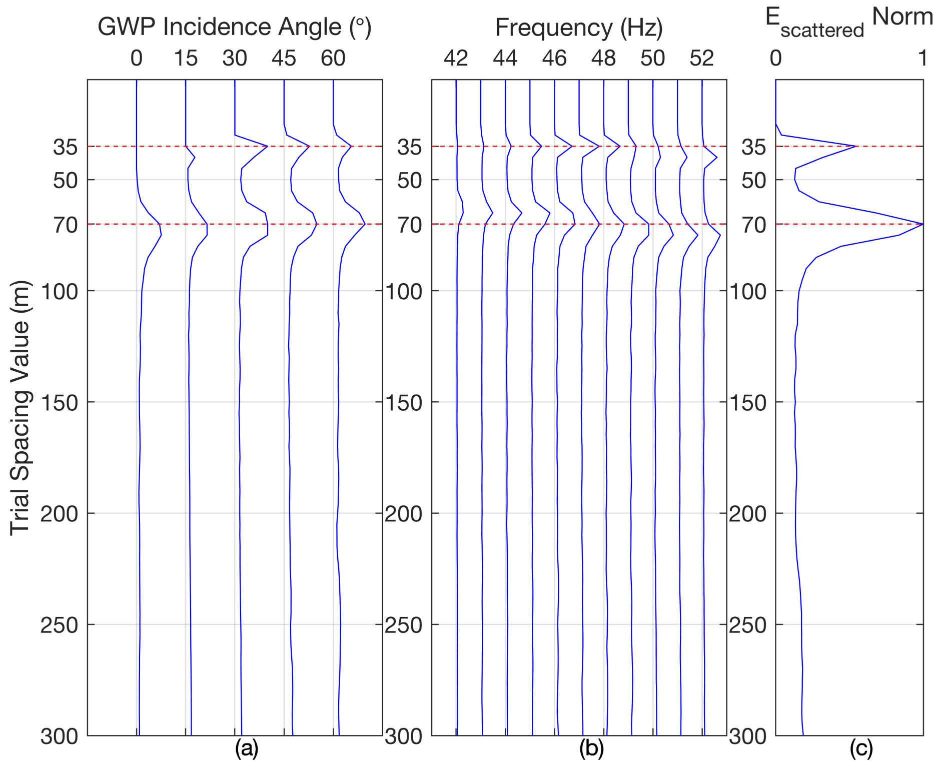

Figure 4.8: (a) $E_{sacttered}(\mathbf{p}_g, \theta)$ for each θ and $\mathbf{p}_g$ by multipling the data values in Figure 4.7 along the axis of frequency. (b) $E_{sacttered}(\mathbf{p}_g, \omega)$ for each θ and $\mathbf{p}_g$ by multipling the data values in Figure 4.7 along the axis of incident angle. (c) The toal $E^{gwp}_{sacttered}(a)$ produced by multipling the traces together either in (a) or (b).

4.4 Numerical examples of the fracture characterization using GWPs

We limit our application to the onshore problems, where most areas have a simple layered structure. Even in such structurally simple media, we have challenges to characterize the reservoir properties inside the layer. To test our algorithm, we create three acoustic models and generate GWP seismic data by propagating the GWP source in the model. The propagation is done with a full-waveform FD method. The sources and receivers are located horizontally from 0 *km* to 5.5 *km* with an interval of 5 m, at the depth of 15 m and 25 m, respectively. We treat the fractures as localized low-velocity (0.5 km/s) anomalies. Each individual fracture has a vertical extent of 20 m and a thickness of one FD spatial grid (5 m). Though such a model is not a realistic representation of thin fractures underground, the wave scattering phenomena should be similar for both thick fractures in numerical simulation and thin fractures in reality. We have not followed the linear-slip boundary condition formulism in representing fractures as in Zheng et al. (2013), because our focus here is to invert for the fracture spacing using GWPs rather than the fracture compliance. The fracture length is 20 m in our model, but the length of fractures will not influence the scattering wave pattern generated by the interferences among individual fractures in a target zone.

In our first example, we add a set of fractures with a constant spacing of 110 m to the third layer (Figure 4.9a). We illuminate the fracture target with five GWP sources. The five GWP sources are constructed with the same GWP parameters ($p = 289, \gamma = 1.2, \varepsilon = 10$) in the first layer. However, their propagation angles are different: 0°, 5°, 10°, 15°, 20°, with respect to the vertical axis. Figure. 4.9b presents the data due to a 0° GWP source (propagation angle 0°). Instead of using the accurate velocity model, we use an inexact model. In this inexact model, each layer thickness does not change, but the velocities are reduced by 20%. The time window determined by this inexact model can still capture the main energy of the multiply scattered waves produced by fractures. We use five incident GWPs of 5 different propagation angles and ten discrete frequencies from 25 Hz to 34 Hz with increment of 1 Hz to calculate the normalized $E^{gwp}_{sacttered}(a)$, which achieves the maximum when the trial spacing a is 110 m, which is the value put in the model (Figure 4.9c).

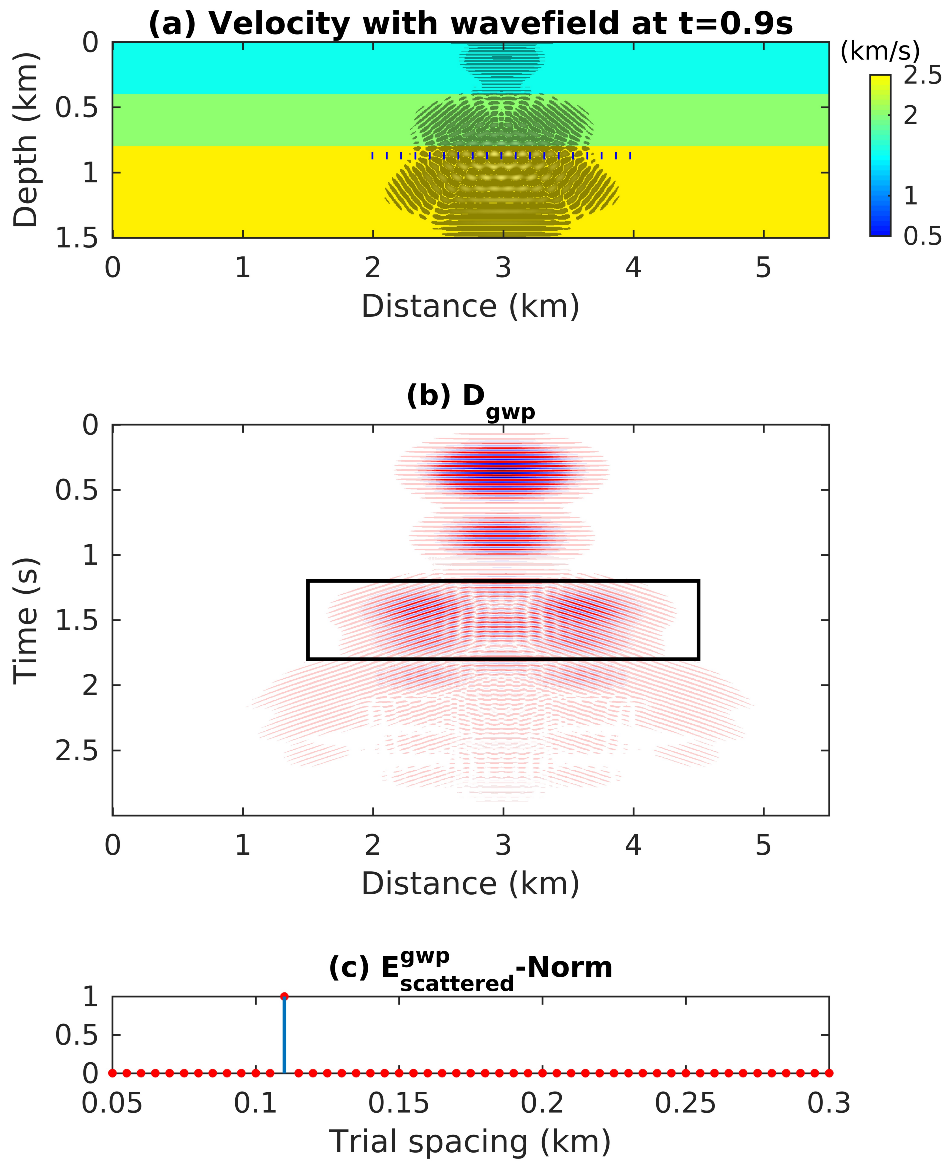

Figure 4.9: (a) A layered velocity model with increasing velocities: 1.5 km/s, 2 km/s and 2.5 km/s. The fracture set has a spacing 110 m located in the third layer. A wavefield snapshot due to a 0-deg GWP is also shown. (b) The modeled GWP-gather D_{gwp} due to a GWP source. The box denotes the scattered data produced by fractures. (c) The normalized $E^{gwp}_{scattered}$ with respect to trial spacing a.

In the second example, we illustrate the effectiveness of using the GWP source (constructed with $p = 289, \gamma = 1.2, \varepsilon = 10$ in a velocity model of 2.5 km/s) to detect multiple fracture sets locally in a constant velocity model (2.5 km/s) (Figure 4.10a). From the left to the right, there are three sets of fractures with different spacings, 160 m, 110 m and 60 m, at a depth 0.75 km. We synthesize the GWP source from different surface locations to illuminate these targets separately. For each set of fractures, the normalized reaches the maximum value at the spacing value 160 m, 110 m and 60 m respectively (Figure 4.10b). Because we only use three propagation angles (0°, 5°, 10°) and seven discrete frequencies (43 Hz to 49 Hz, with increment of 1 Hz), the normalized $E^{gwp}_{scattered}$ may give other values around the true spacing.

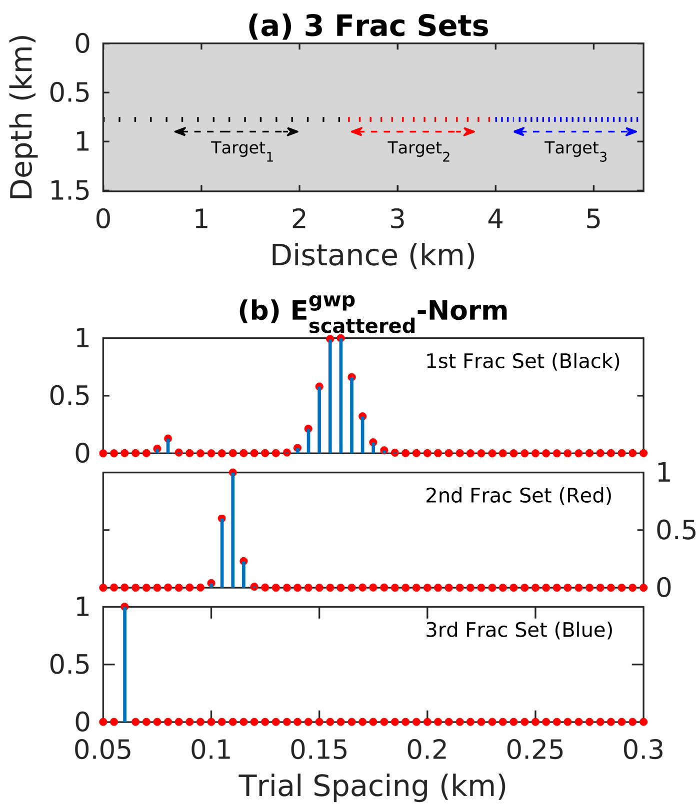

Figure 4.10: (a) Three sets of fractures (different colors) located as the same depth 0.75 km in a constant velocity model (2.5 km/s). For distance 0-2.5 km, 2.5-4 km and 4-5.5 km, the spacing interval is 160 m, 110 m and 60 m respectively. The three targets are shown within the double arrows. (b) The normalized $E^{gwp}_{scattered}$ for the three sets of fractures.

In our third example, we demonstrate how GWPs can be used to distinguish two sets of fractures at different depths in a constant velocity model. The first set is located at a shallower depth (0.8 *km*) and has a spacing of 110 *m* and the deeper set (depth of 1.2 *km*) has a spacing of 60m (Figure 4.11a). To detect the fractures in a targeted area (Figure 4.11a), we illuminate them with the GWP from five propagation directions (0°, 5°, 10°, 15°, 20°). For each angle, we have ten discrete frequencies (43 *Hz* to 52 *Hz*, with increment of 1 *Hz*) to calculate $E^{gwp}_{scattered}$. In this targeted area, the normalized $E^{gwp}_{scattered}$ shows its maximum at the true fracture spacings 110 *m* and 60 *m*, respectively (Figure 4.11b).

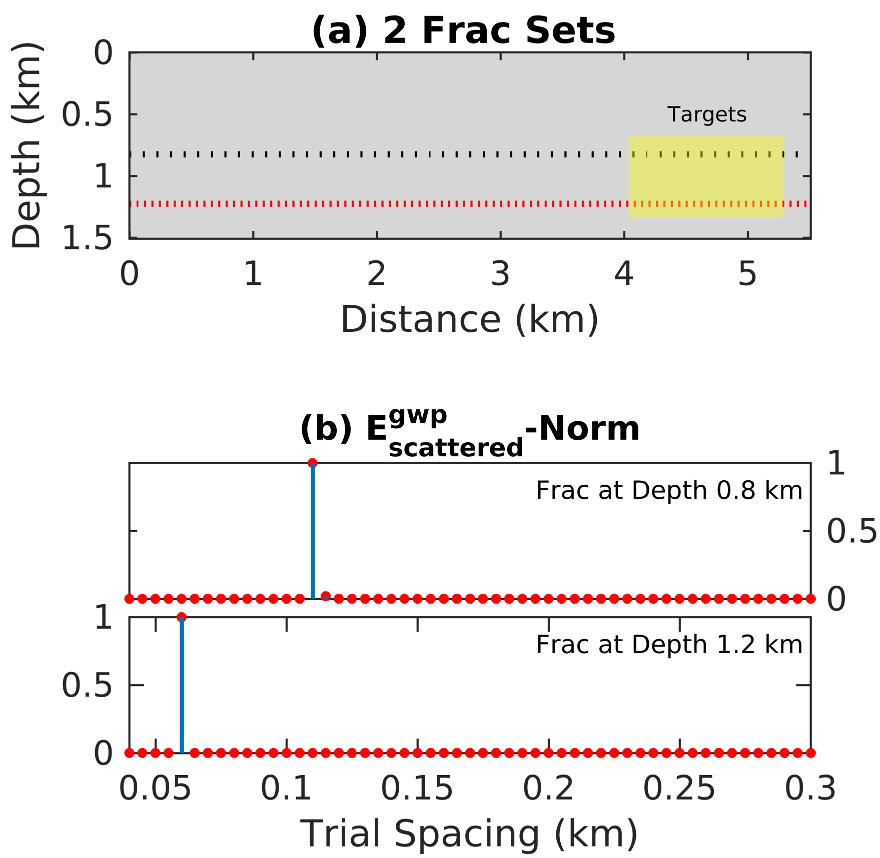

Figure 4.11: (a) Two sets of fractures with spacing 110 *m* and 60 *m* located at depth 0.8 *km* and 1.2 *km*, respectively, in a homogenous model (v=2.5 km/s). The yellow area shows the targeted fractures. (b) The normalized $E^{gwp}_{scattered}$ for the two sets of fractures.

4.5 Discussion

The ability to decompose the seismic wavefield into a set of localized and directional packets, as shown in this study, is of great importance in seismic imaging and inversion (Nowack, 2012). The GWP we used is an object in the phase space and the phase-space approach has been proven to be very useful in seismic imaging (De Hoop et al., 2000; Fishman, 2002; Wu, 2003).

It provides us a new view on seismic imaging, analogous to the experiment setup in the high-energy particle physics: a physicist would shoot a stream of directional particles to bombard a target to interrogate its composition and structure by studying the scattering. The "particle" for seismic imaging here is the recently proposed GWP, whose spatial localization and directional properties allow us to control its interaction with only selected targets. In contrast, a point-source wavefield will interact with all subsurface objects and creates various interferences such as multipathing that may inhibit our ability to infer the structures around the target.

Though we only demonstrated our fracture characteriztion method in the 2D acoustic media, it is possible to apply the method to characterize the fracture networks of which the host media are 2D elastic ones, either isotropic or anisotropic. The plane wave scattering theroy still holds in the elastic media, but we need to find the correct wavenumber of the scattered waves based on different wave types (P wave or S wave) and/or different wave propagation direction. To obtain the correct wavenumber for the scattered waves, we can solve the boundary conditions on the interface below which is the media hosting fracture networks.

4.6 Conclusions

Based on plane wave scattering theory, we developed a procedure for fracture inversion using GWPs. Our fracture inversion algorithm can invert for fracture density in different cases, including that with a single set of parallel fractures of uniform fracture spacing, a set of parallel fracture with spatially variable spacing, and that with two sets of fractures located at two different depths in the subsurface. In addition, our new method can tolerate significant errors in the velocity model, as demonstrated in the synthetic examples.

5 Faults imaging using second-order scattered waves

5.1 Introduction

Imaging faults accurately is fundamental in geological interpretation of petroleum system development and energy exploration and development. Due to limitations within traditional seismic imaging methods, faults in the seismic images are usually interpreted/delineated by interpreters or by specific post-stack processing methods by studying image attributes (e.g., Cohen et al., 2006; Hale, 2013b; Wu and Hale, 2016a,b). In exploration seismology, there are two main reasons why faults are rarely directly imaged in traditional RTM imaging methods (Baysal et al., 1983). Firstly, conventional imaging methods only treat single scattering events (primary reflections) as useful signals when forming the subsurface image. Secondly, since the faults usually have high dipping angles and the seismic acquisition aperture is limited, primary reflections from the fault planes cannot propagate back to geophones located on the surface. Imaging high-angle faults needs multiple scattering events (e.g., (Zuberi and Alkhalifah, 2014)). We hereby introduce a modified RTM method to utilize the second order scattering events (multiples) (He and Wu, 2009) reflected from the fault plane. He and Wu (2009) used the seismic interferometric virtual source idea (Wapenaar, 2004; Schuster et al., 2004; Schuster and Snieder, 2009; Zheng and He, 2010; Zheng, 2010; Bakulin and Calvert, 2006)(Wapenaar, 2004; Schuster, 2001; Schuster, 2009; Zheng, 2010; Zheng & He, 2010; Bakulin & Calvert, 2006) to first focus the wavefield to a subsurface point. The difference is that they focus the field to a real scattering point. Here, we propose a different approach using scattered energy to do imaging. We first run traditional RTM in the initial migration velocity model to obtain an image from which we can identify scattering points/reflectors. We then modify the migration velocity model by adding some horizontal reflector/scatters identified in the previous step. We do the RTM imaging again. During the second iteration of RTM, we run the forward (or backward) propagation in the original velocity model but run the backward (or forward) propagation in the modified velocity model. In this way, we are able to image the fault planes directly. The added sub-horizontal reflector is readily obtainable in the traditional RTM image. We can calculate the local velocity (or density) perturbation from the reflectivity horizon in the image. This calculated local velocity (or density) perturbation is the reflector we add into the smoothed migration velocity. We demonstrate with two numerical examples that our asym-RTM method can image the fault directly.

5.2 Review of RTM

Our modified RTM is based upon the principles of conventional RTM. Before presenting our modified RTM (the asym-RTM), we first list the basic assumptions of the RTM imaging method. We use a simple model to illustrate the strengths and weaknesses of traditional RTM. The model is a constant velocity model that has two reflectors: the horizontal R1 and the vertical R2 (Figure 5.1a).

In implementing the traditional RTM, there are three inputs: source, data, and a migration velocity model. The migration velocity is a smoothed velocity model without any distinctive boundaries. Conducting RTM in the following three steps, we can get the image.

Step 1. Forward modeling of the source field (Figure 5.1b): we propagate the source signal at location xs to every subsurface point x in the migration velocity model. We simply consider the source wavelet as a Delta function through the paper. The source wavefield can be expressed as the Greens $G(\mathbf{x}, \mathbf{x}_s, \omega)$ in the frequency (ω) domain.

Step 2. Backward extrapolation of recorded data (Figure 5.1b): we propagate the time-reversed data $D(\mathbf{x}, \mathbf{x}_g, \omega)$ in the same migration velocity as in Step 1.

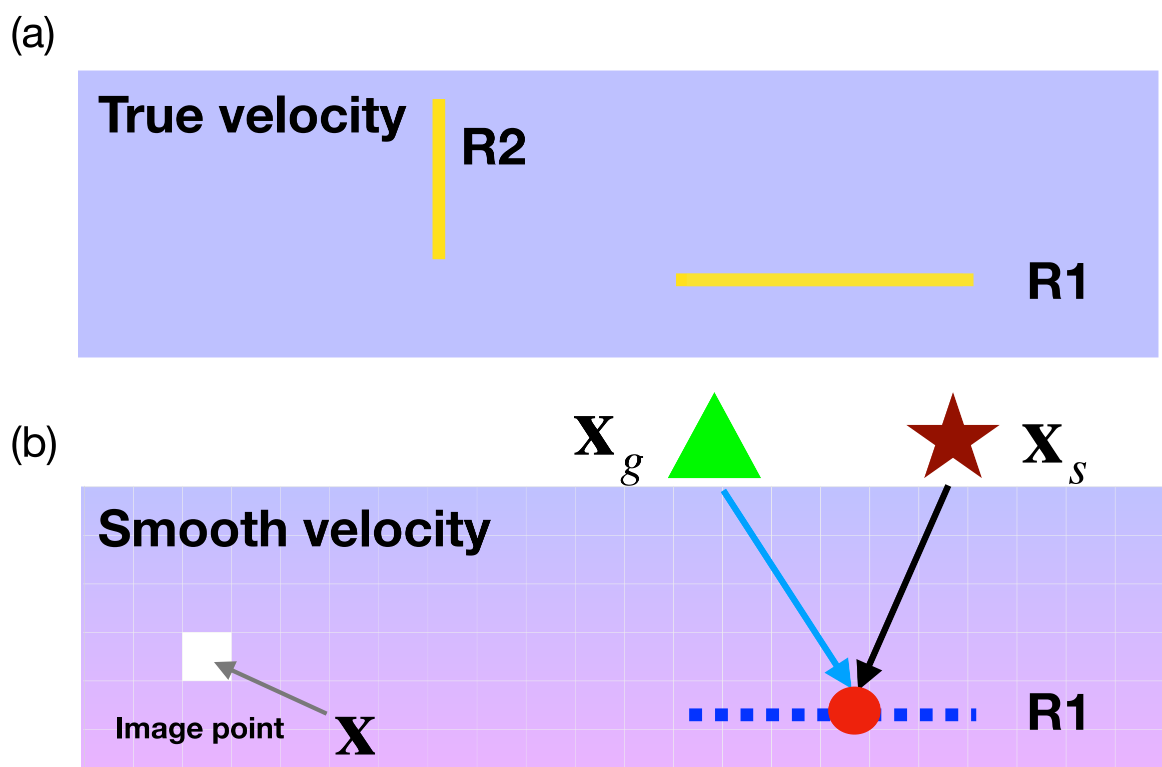

Figure 5.1: Traditional RTM: (a) A constant background velocity model (rectanglar block) having two reflectors (R1 & R2, yellow bars). (b) Conventional RTM in the smoothed velocity model, the red dot is the image produced by raypaths from backward propagation (Blue) and forward propagation (Black). Note that the blue dotted line in (b) is the imaged R1 by traditional RTM in the smoothed velocity model.

Step 3. Imaging condition (Figure 5.1b): we can form an image $I(\mathbf{x})$ at every location $\mathbf{x}$ by cross-correlating the wavefield from the source side and the wavefield from receiver side:

$$I(\mathbf{x}) = \sum_{\omega}\sum_{\mathbf{x}_s}\sum_{\mathbf{x}_g} G(\mathbf{x},\mathbf{x}_s,\omega)D^*(\mathbf{x},\mathbf{x}_g,\omega) \tag{5.1}$$

in which D^* is the complex conjugate of data D. To simplify the equations, we omit variable ω in future equations. The image formed in Step 3 only has the horizontal reflector R1, while the vertical reflector R2 is not observable using the conventional RTM. We show such an image in our later section **Numerical examples**.

5.3 Asymmetrical RTM

We propose a modified RTM method based on the foundations of conventional RTM. In our modified RTM method, we perform RTM algorithms twice to utilize second order events into the imaging. The first-time running of RTM is to image the sub-horizontal reflectors. The second-time running of RTM is to image the vertical/steep reflectors, with the aid of sub-horizontal reflectors.

The procedures for our modified RTM method can also be categorized into 3 steps.

Step 1. Initial RTM: we first perform traditional RTM in the smoothed migration velocity to obtain the image $I(\mathbf{x})$. In the image, sub-horizontal reflectors like R1 (Figure 5.1) is imaged. The reflector R1 in the image is the source-wavelet- modified reflectivity. Assuming the source wavelet is a Delta function, the image can represent the reflectivity. Treating the reflectivity for each image point as that obtained at the zero degree incidence, we express the reflectivity (r_1) in terms of the impedance Z:

$$r_1 = \frac{Z_1 - Z_2}{Z_1 + Z_2} \tag{5.2}$$

where the impedance Z is the scalar product of density ρ and velocity V. Z_1 and Z_2 are impedances above and below the reflector, respectively.

Step 2. Injection of reflectivity into the model: Assuming Z_1 is the background impedance at the imaged reflector, we write Z_2 as Z_1 plus an impedance perturbation term dZ. Using Eq. 5.2 we calculate the impedance perturbation term:

$$dZ = -\frac{2Z_1 r_1}{1 - r_1} \tag{5.3}$$

If we further treat the density as a constant around the imaged reflector, we get the velocity perturbation:

$$dV = \frac{dZ}{\rho_1} = -\frac{2V_1 r_1}{1 - r1} \tag{5.4}$$

Similarly, we can treat the velocity as a constant around the imaged reflector, we get the density perturbation:

$$d\rho = \frac{dZ}{V_1} = -\frac{2\rho_1 r_1}{1 - r1} \tag{5.5}$$

Based on Eq. 5.4 and Eq. 5.5, we have transferred the reflectivity (r_1) in image domain into the model parameter perturbation (dV or dρ) in the model domain.

In our study, we keep the density model unchanged and calculate the dV. We define dV as the reflector $R1_{cal}$:

$$R1_{cal} = dV = -\frac{2Z_1 r_1}{1 - r1} \tag{5.6}$$

We then add the reflector $R1_{cal}$ into the smoothed velocity model to construct a new migration velocity model (Figure 5.2).

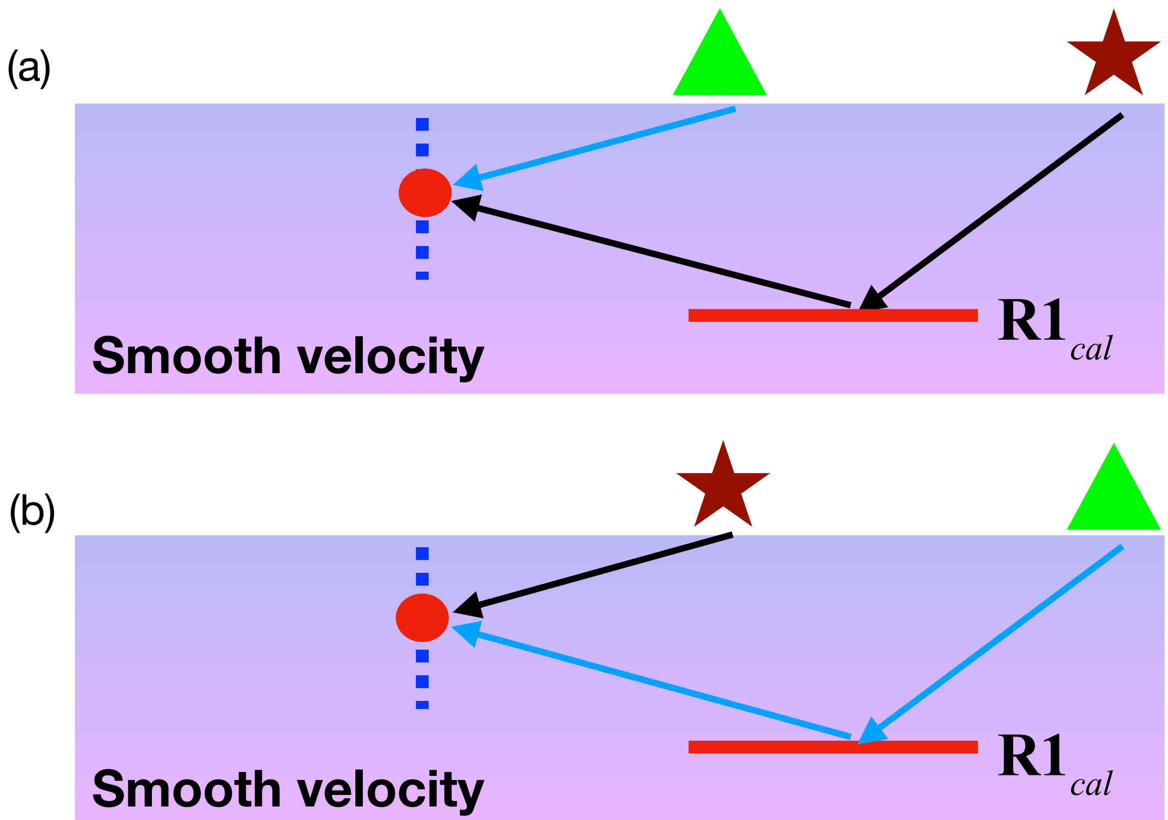

Figure 5.2: Modified RTM: (a) the reflector R1 added in the migration velocity for proapgating the source. (b) the reflector R1 added in the migration velocity for propagating the time-reversed data. The black arrows show the raypaths from the source side; the blue arrows show the raypaths from the receiver side; the red dots are the images produced by waves from the plotted ray paths; and the blue dotted lines indicate the images formed using second order scattering events.

Step 3. Asymmetric RTM: We run the RTM for the second time. The backward modeling is still done in the previous migration velocity, but the forward modeling is performed in the newly modified migration velocity, which has $R1_{cal}$ (Eq. 5.6) in it (Figure 5.2a). In forward modeling, the source wavefield will reflect off the added reflector (Figure 5.2a). Cross-correlating these two wavefields, we form the image $I_{fwd}(\mathbf{x})$ with both the first order scattering events (primary reflections) and second order scattering events (multiples):

$$\begin{aligned} I_{fwd}(\mathbf{x}) &= I_{fwd}(\mathbf{x}) \\ &\quad + \sum_{\mathbf{x}_s}\sum_{\mathbf{x}_g} G(\mathbf{x},\mathbf{x}_R 1)R_{cal}(\mathbf{x}_R 1)G(\mathbf{x}_R 1,\mathbf{x}_s)D^*(\mathbf{x},\mathbf{x}_g) \end{aligned} \tag{5.7}$$

Vice versa, second order scattering events can also be incorporated by forward modeling and backward modeling in the previous smoothed velocity model and the new migration velocity model (Figure 5.2b), respectively. We then form the image $I_{bwd}(\mathbf{x})$:

$$\begin{aligned} I_{bwd}(\mathbf{x}) &= I_{fwd}(\mathbf{x}) \\ &\quad + \sum_{\mathbf{x}_s}\sum_{\mathbf{x}_g} G(\mathbf{x},\mathbf{x}_s)G^*(\mathbf{x},\mathbf{x}_R 1)R_{cal}(\mathbf{x}_R 1)D^*(\mathbf{x}_R 1,\mathbf{x}_g) \end{aligned} \tag{5.8}$$

Based on our modified RTM, we get three images: $I(\mathbf{x})$, $I_{fwd}(\mathbf{x})$, and $I_{bwd}(\mathbf{x})$. We extract the image formed by the second order scattering events:

$$I_{fwd}^{2nd\_Order}(\mathbf{x}) = I_{fwd}(\mathbf{x}) - I(\mathbf{x}) \tag{5.9}$$

and

$$I_{bwd}^{2nd\_Order}(\mathbf{x}) = I_{bwd}(\mathbf{x}) - I(\mathbf{x}) \tag{5.10}$$

The amplitudes of the second order scattering events are usually smaller with orders of magnitudes, when compared with the amplitudes of the first order scattering events. Thus, the image

$I_{fwd}^{2nd\_Order}(\mathbf{x})$ is also smaller with orders of magnitudes than the image $I(\mathbf{x})$. To enhance the image $I_{fwd}^{2nd\_Order}(\mathbf{x})$, we multiply it with a scaling factor (A). Then, we sum the scaled $I_{fwd}^{2nd\_Order}(\mathbf{x})$ and $I(\mathbf{x})$ to form a final image:

$$I_{fwd}^{final}(\mathbf{x}) = AI_{fwd}^{2nd\_Order}(\mathbf{x}) + I(\mathbf{x}) \tag{5.11}$$

The same process is applied to $I_{bwd}^{2nd\_Order}(\mathbf{x})$:

$$I_{bwd}^{final}(\mathbf{x}) = AI_{bwd}^{2nd\_Order}(\mathbf{x}) + I(\mathbf{x}) \tag{5.12}$$

5.4 Numerical examples

5.4.1 Step model

First, we use a two-layered velocity to test our method. There is a vertical step along the velocity boundary in the model (Figure 5.3a). The grid points in the model are distributed as 408 vertically and 906 horizontally. The gird size is 10 *m*. There are 303 sources locate from 0 *km* to 9.05 *km*, with an interval of 30m. We deploy 906 receivers from 0 *km* to 9.05 *km* with an interval of 10 *m* to record data for every source. Both sources and receivers are at depth of 50 *m*. The source signal is a Ricker wavelet. Its main frequency is 30 *Hz*. The total recording time length is 3.6 *s*.We use the velocity in the first layer (1.5 km/s) as the migration velocity (Figure 5.3b) for the traditional RTM. Adding the velocity anomaly (2.5 km/s) as the reflector into the migration velocity (Figure 5.3b), we obtain the modified migration velocity (Figure 5.3c). This added reflector is obtained from one reflectivity horizon in the traditional RTM image (Step 1&2 in Modified RTM).

For the traditional RTM, we run the forward modeling and backward modeling in the migration velocity (Figure 5.3b) and form the image $I(\mathbf{x})$ (Figure 5.3d) following the imaging condition (Eq. 5.1). While the horizontal boundary is imaged clearly, the step of the boundary fails to be imaged. In our modified RTM, we acquire two images $I_{fwd}^{final}(\mathbf{x})$ (Figure 5.3e) and $I_{bwd}^{final}(\mathbf{x})$ (Figure 5.3f), based on Eq. 5.11 and Eq. 5.12. The step boundary is clearly imaged in both images.

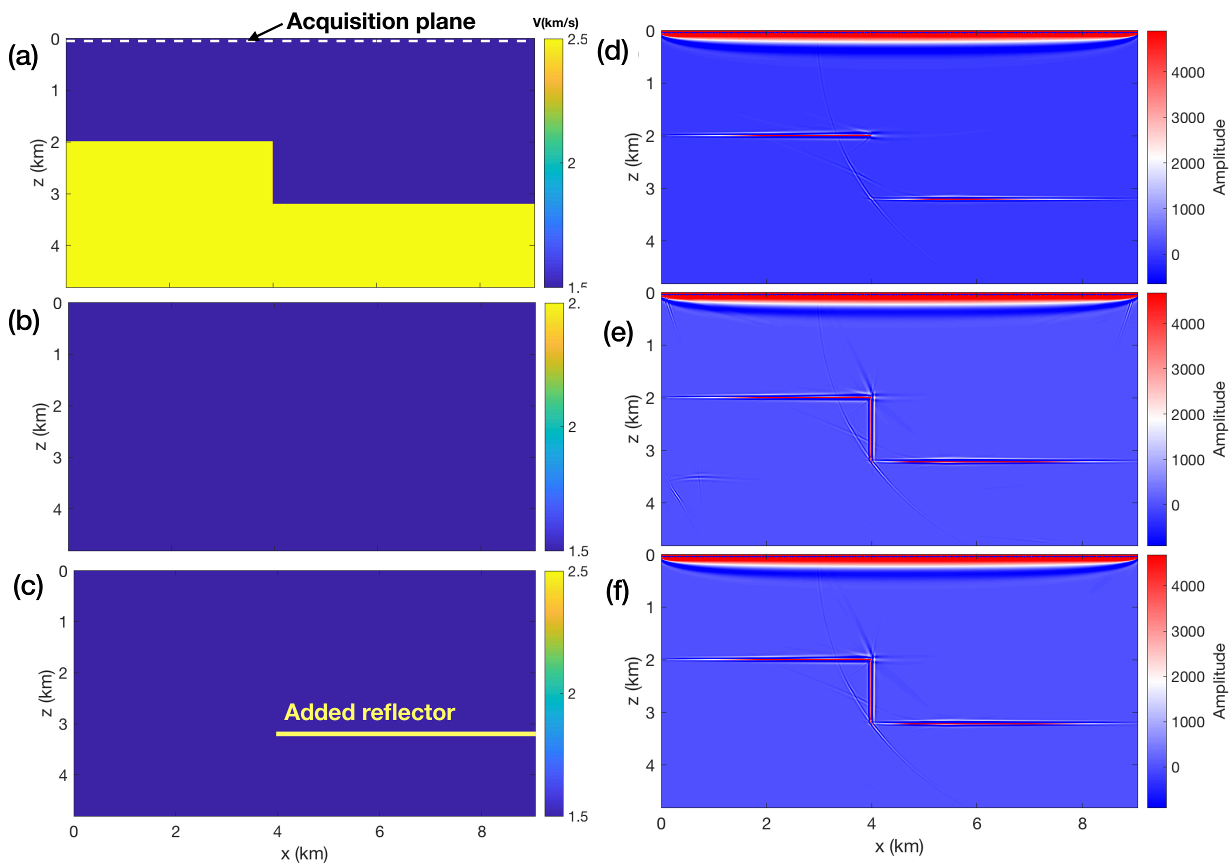

Figure 5.3: (a) Two-layered(1.5km/s & 2.5 km/s) velocity model. (b) Constant migration velocity (1.5 km/s). (c) Modified migration velocity, with an added reflector. (d) Traditional RTM image I. (e) Modified RTM image I_{fwd}^{final}. (f) Modified RTM image I_{bwd}^{final}.

5.4.2 Fault model one

In our second example, we use a multi-layered model (Figure 5.4a) with a vertical fault in the middle. The fault is located at x = 4 *km*. This velocity model is similar to the model in Figure 13 used by Malcolm et al. (2009). The model consists of a 400 by 800 grid. The grid size is 10 *m*.

The 400 sources range from 0 *km* to 7.8 *km*. For each source, there are 400 receivers ranging from 0 *km* to 7.8 *km*. Both the sources and the receivers have a constant interval of 20 *m*. They are both located at the depth of 50 *m*. The source signal is a Ricker wavelet. It has a main frequency of 15 *Hz*. The total recording time length is 5 *s*.

For traditional RTM imaging, we use the smoothed migration velocity (Figure 5.4b) to run the forward and backward modeling. For the modified RTM, we build a modified migration velocity (Figure 5.4c) for forward modeling. There is a strong reflector in the model that can be easily picked out from the image of traditional RTM. For backward modeling, we still use the smoothed migration velocity (Figure 5.4b). In the modified RTM method, we get the image using Eq. 5.11.

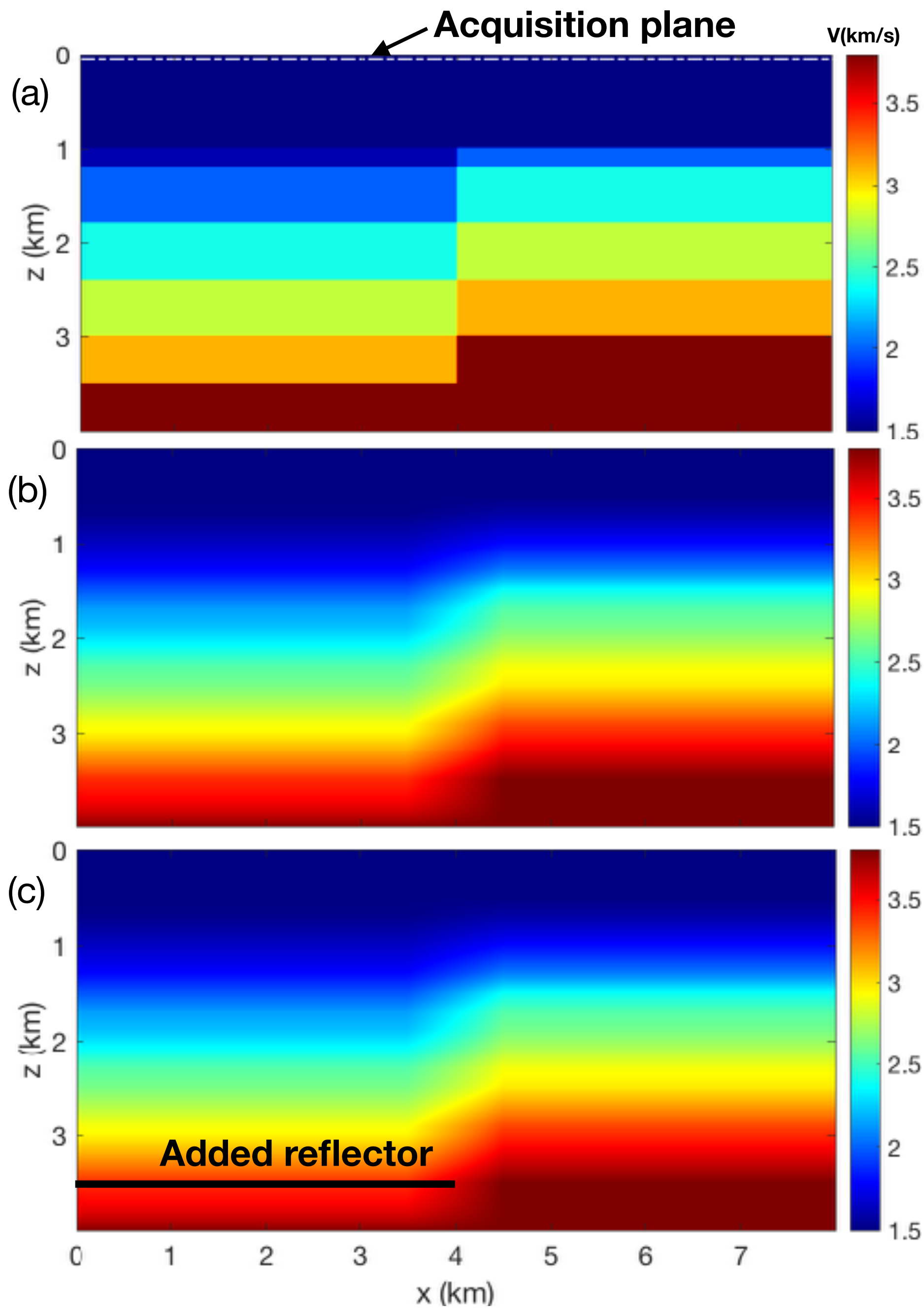

Figure 5.4: (a) True velocity model. The dashed line indicates the acquisiotn plane. (b) Smoothed migration velocity. (c) Modified migration velocity with a reflector added.

In the traditional RTM image (Figure 5.5a), the fault is not clearly imaged. In comparison, for the modified RTM image (Figure 5.5b), the fault is easily observable.

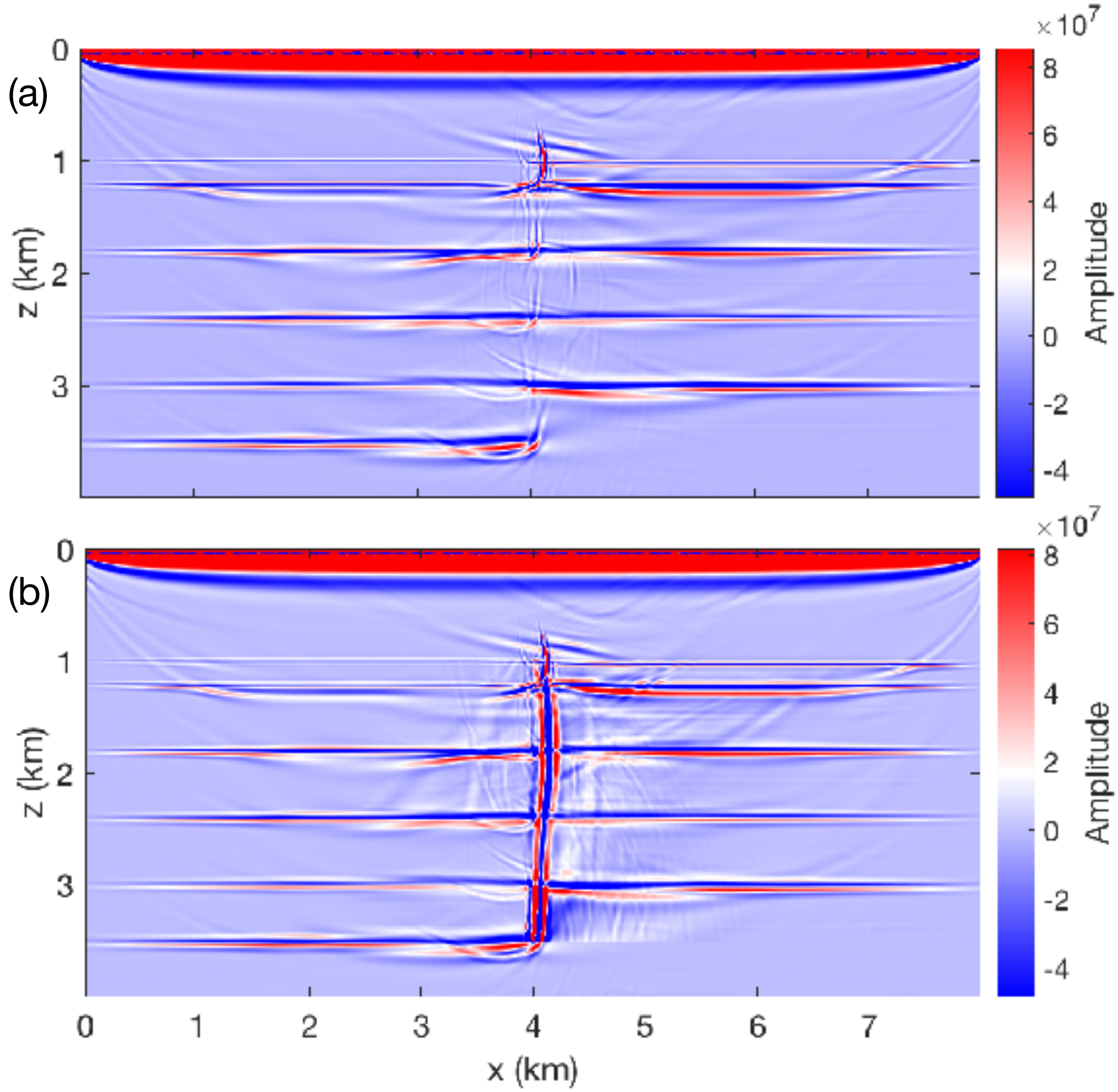

Figure 5.5: (a) Traditional RTM image I. (b) Modified RTM image I_{fwd}^{final}.

5.4.3 Fault model two

In our third numerical example, the high-angle fault model (Figure 5.6) is built from a partial area in the acoustic Marmousi model. The fault model is 3 *km* vertically and 4 *km* horizontally. The grid size is 10 *m*. There are 100 sources evently distributed along the surface. For each source, there are 200 receivers from 0 *km* to 3.98 *km* with a constant interval of 20 *m*.

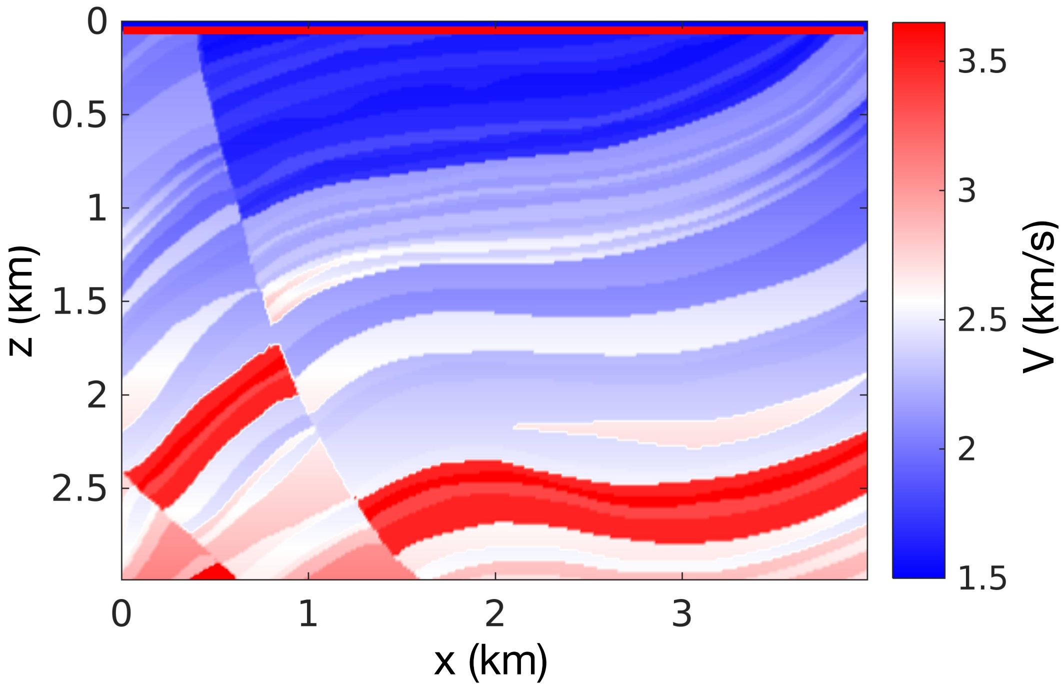

Figure 5.6: True velocity model. The red line at the top denotes the acquisition plane.

We produce a reflectivity model (Figure 5.7) using the velocity model and the constant density model (1 kg/m^3). Convolving a source wavelet with the vertical reflectivity model (Figure 5.7), we produce a zero-offset image (Figure 5.8) as a benchmark image for the conventional RTM image and the asymmetrical RTM image.

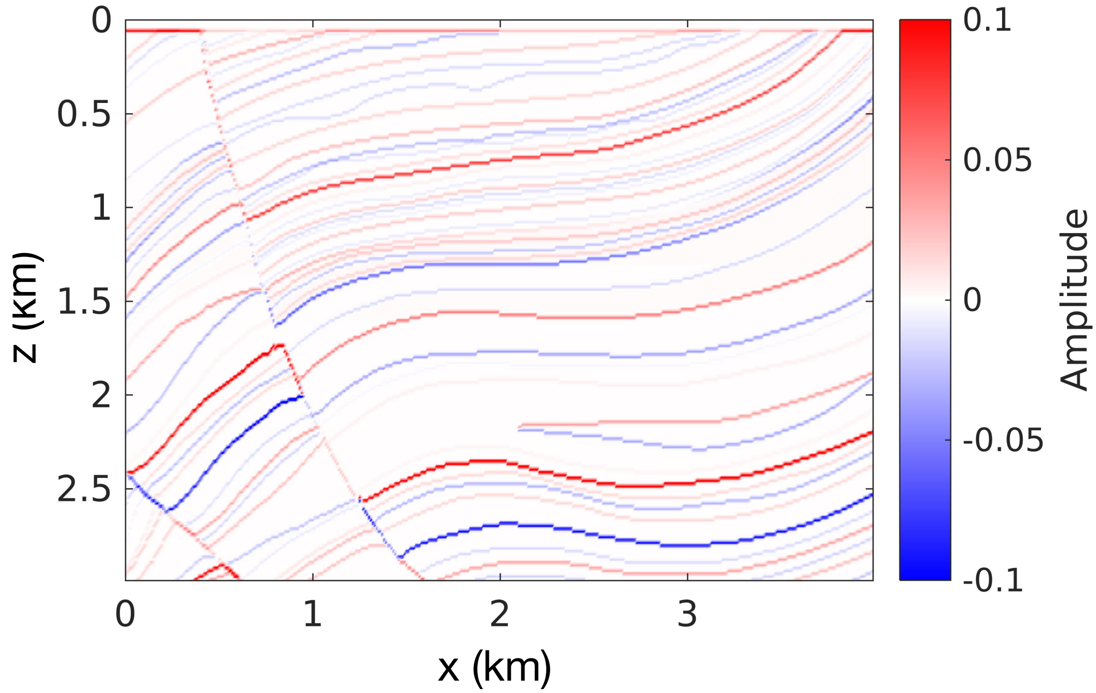

Figure 5.7: Reflectivity model which is derived from the true velocity model in Figure 5.6.

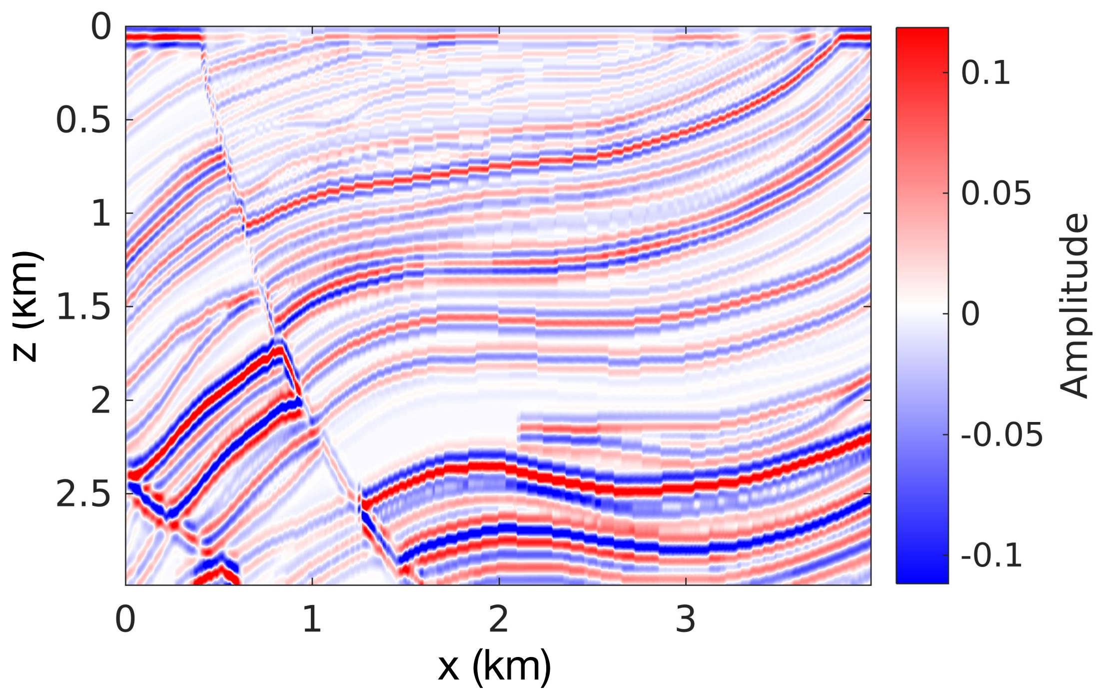

Figure 5.8: Zero-offset RTM image from the reflectivity model in Figure 5.7.

The smoothed velocity model (Fiugre 5.9) is acquired by smoothing the origional velocity model using a 2D Gaussian smooth function. We ran the traditional RTM algorithm using the smoothed velocity model to produce an RTM image (Figure 5.10). The RTM image showed clearly on the sub-horizontal reflections along the horizontal axis from 1 *km* to 3.98 *km*. However, the steep fault that went through from the top part to the base part of the model was hard to be imaged. It would be difficult to interpret the fault location just based on the traditional RTM image (Figure 5.10).

Based on the asymmetrical RTM method, we were able to utilize the second scattered waves to image the high-angle fault. By extracting different reflectors in the tradtional RTM image and add the corresponding velocity perturbations at different depths, we could use the different second order scattered waves to image the specific part of the fault. The first reflecor (**reflector01**) we extracted from the image is at a depth of around 2.5 *km*. Then we added velocity perturbation at this reflector location in the velocity model. The amplitudes of the velocity perturbation is propotional to the positive amplitudes along the reflector in the RTM image (Figure 5.10). Using the modified velocity model (Figure 5.11), The modified RTM image $I_{fwd01}^{2nd\_Order}$ (Figure 5.12) of the fault using Eq. 5.11 was obtained. The lower part of the fault plane was imaged clearly in $I_{fwd}^{2nd\_Order}$ (Figure 5.12). Similarly, we chose the second reflector (**reflector02**) at a shallow depth to image the shallow part of the fault. Using the modified velocity with the velocity perturbation added at the location of **reflector02** (Figure 5.13), we imaged the shallow part of the fault $I_{fwd02}^{2nd\_Order}$ (Figure 5.14) successfully.

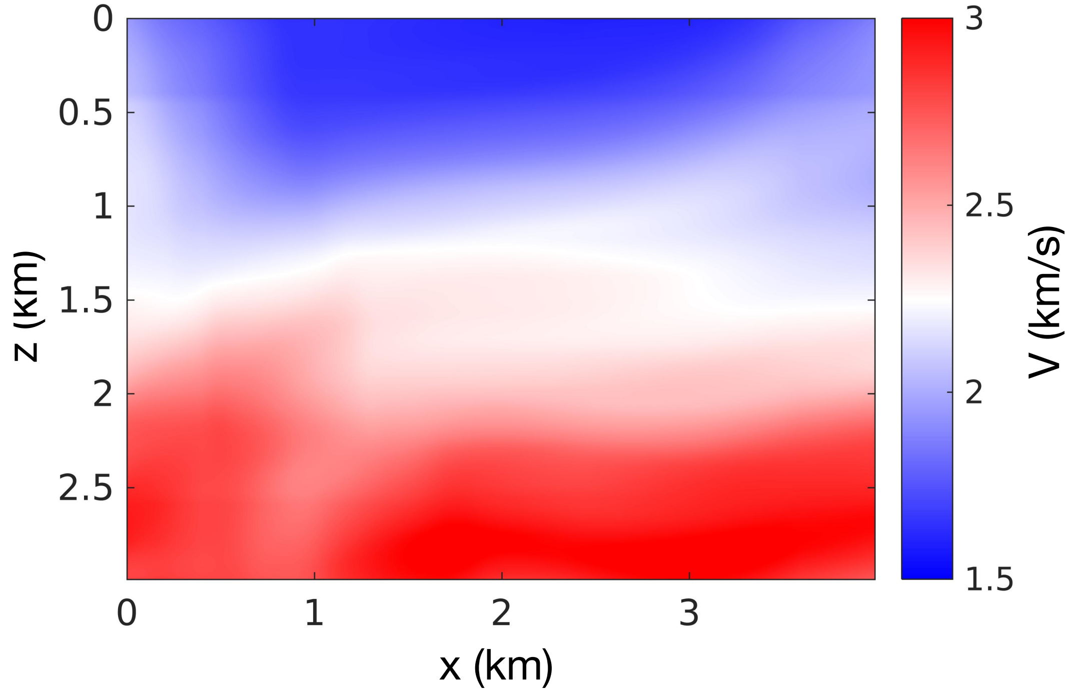

Figure 5.9: Smoothed velocity model.

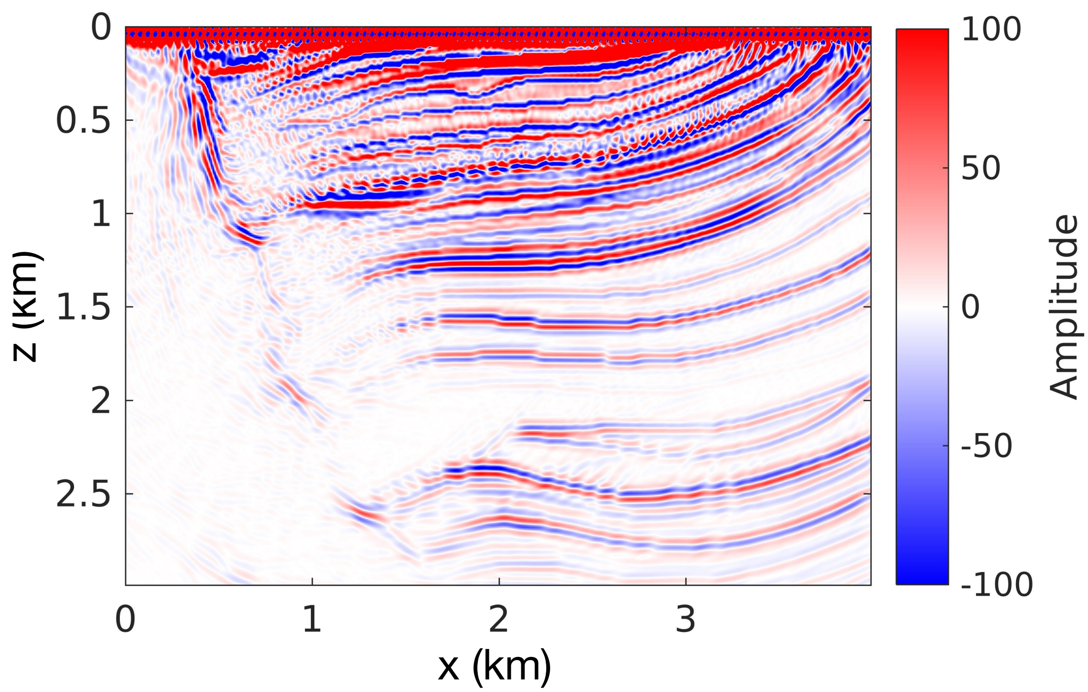

Figure 5.10: Traditional RTM image from the smoothed velocity model.

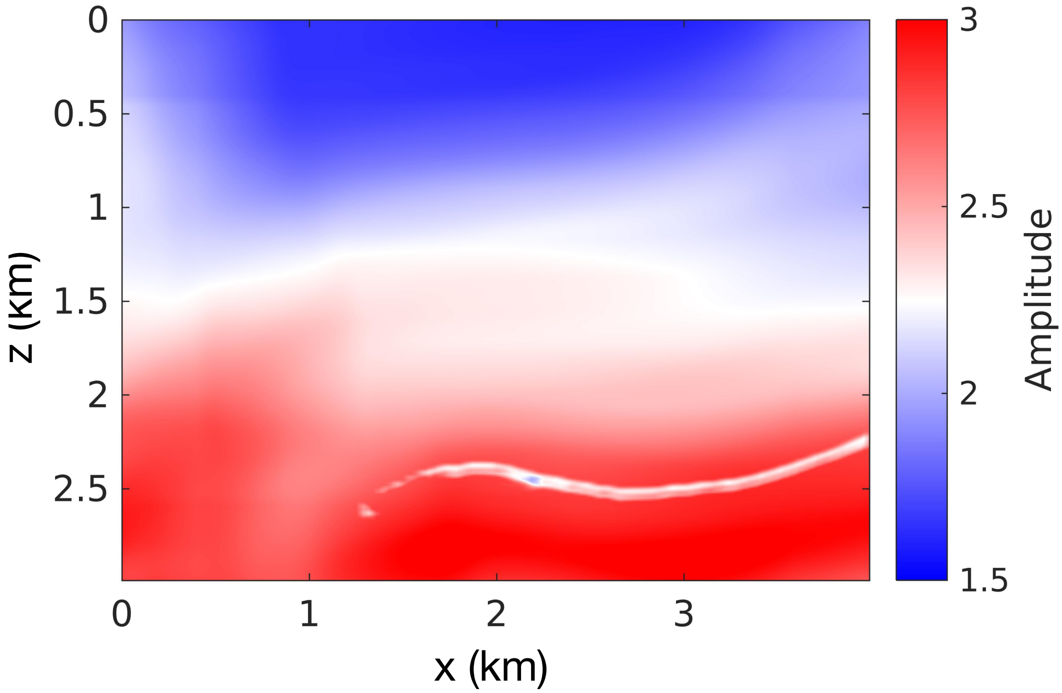

Figure 5.11: Modified velocity model by adding velocity perturbations at the location of **reflector01**.

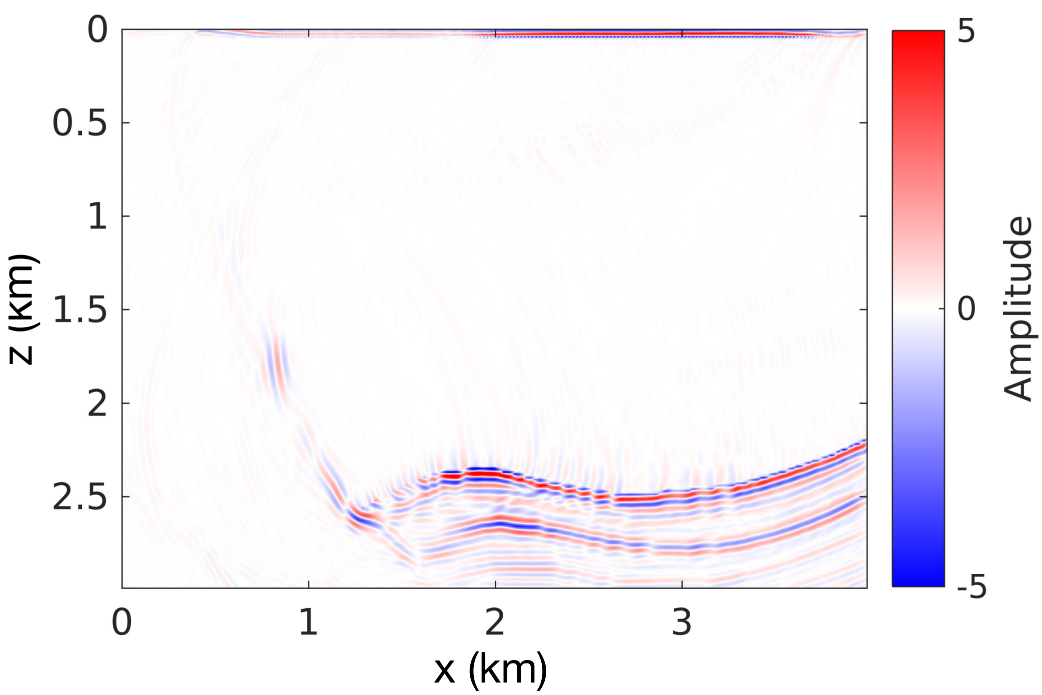

Figure 5.12: Modified RTM image $I_{fwd01}^{2nd\_Order}$ using velocity model in Figure 5.11.

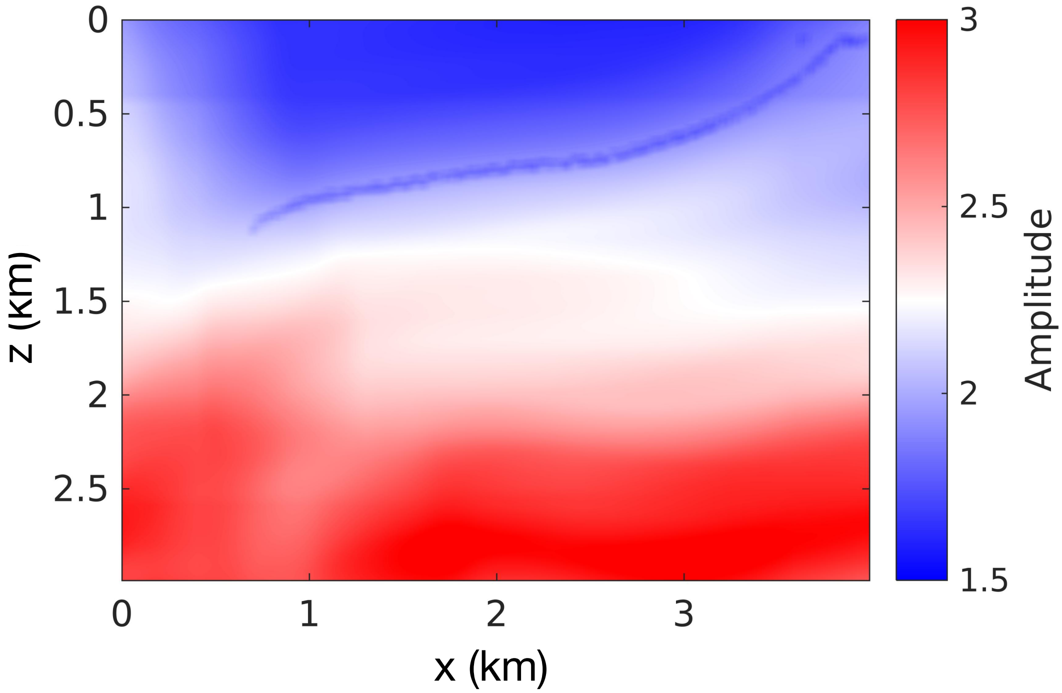

Figure 5.13: Modified velocity model by adding velocity perturbations at the location of **reflector02**.

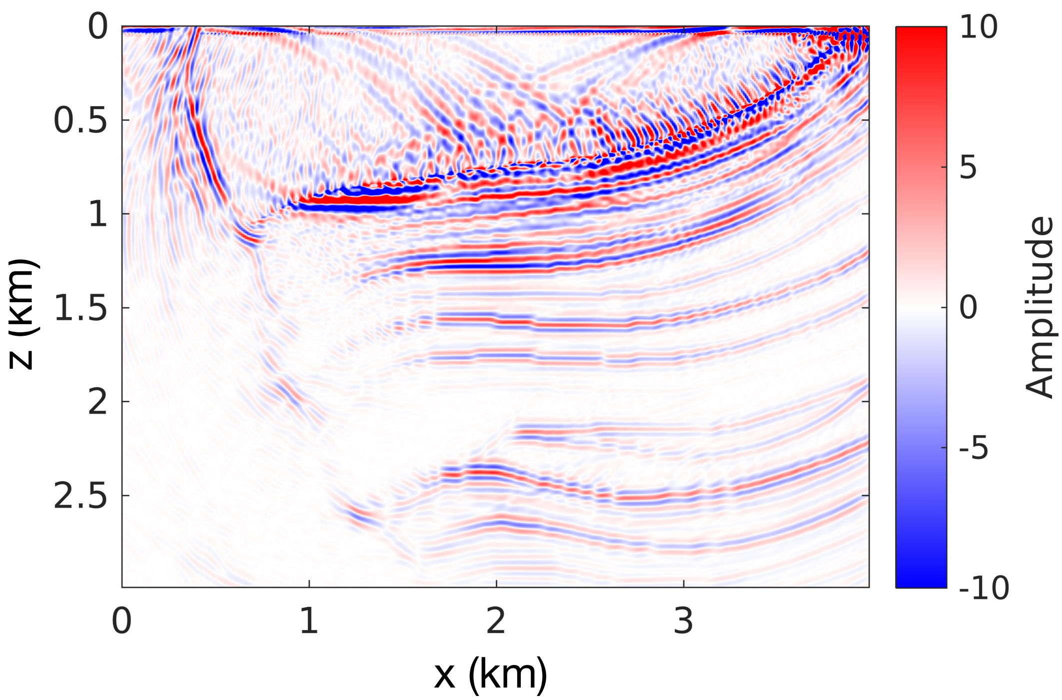

Figure 5.14: Modified RTM image $I_{fwd02}^{2nd\_Order}$ using velocity model in Figure 5.13.

Summing the images $I_{fwd01}^{2nd\_Order}$ and $I_{fwd02}^{2nd\_Order}$ together, we formed the final image $I_{fwd_{final}}^{2nd\_Order}$ (Figure 5.15). Compared with the traditional RTM image (Figure 5.10), the image $I_{fwd_{final}}^{2nd\_Order}$ shows the fault reflection clearly to assist the geological interpretation. Based on this example, we showed that it is possible to utilize the second order scattering waves and image the steep fault in a relative complex geological model.

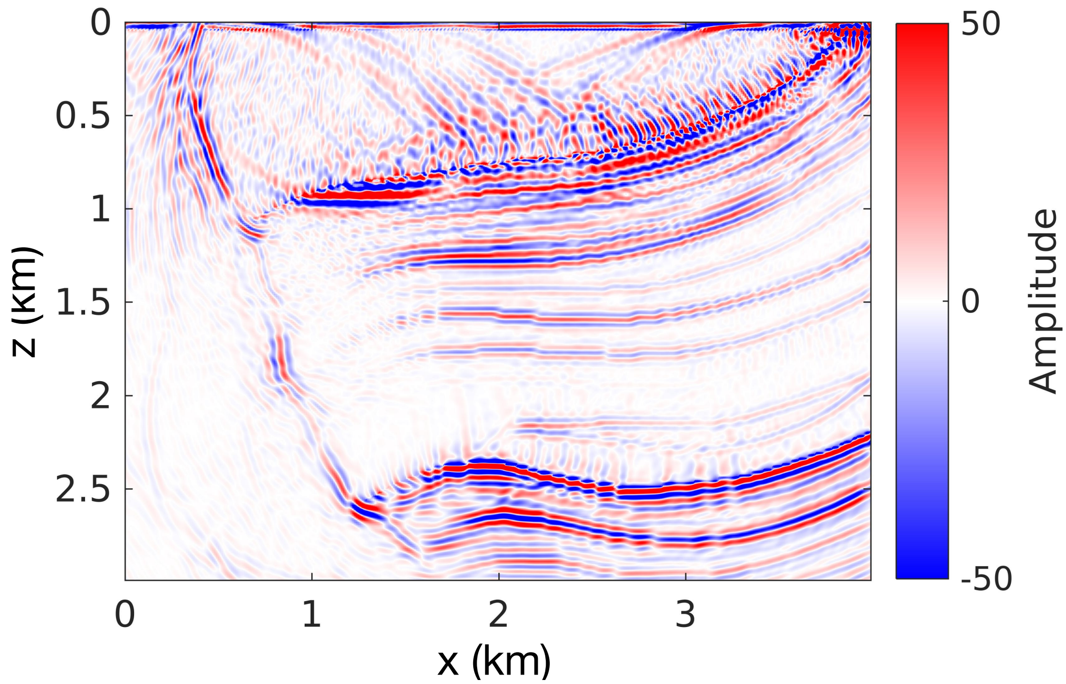

Figure 5.15: Modified RTM image $I_{fwd_{final}}^{2nd\_Order}$.

5.5 Discussion

High-fidelity imaging of high-angle faults in the subsurface is a challenging topic in seismic imaging industry even if we were given the correct migration velocity and accurate reverse time migration (RTM) operator. We showed a simple modified RTM method to image the vertical fault planes. The success of the modified RTM method is due to that a previously imaged reflector is added into the velocity model as a perturbation of the smooth background velocity. Such an additional information of the velocity model contributes to utilizing the second order scattering waves in our proposed asymmetrical RTM. In the traditional imaging methods, primary reflections are assumed to be the only useful information when forming an image. Multiples are considered as noise and removed during the pre-processing. However, in our asymmetrical RTM, the second-order scattering waves are considered as signal to delineate high-angle faults. It provides a new way to exploit multiples in imaging just by velocity model building, which can be easily adapted to the current imaging algorithms.

5.6 Conclusions

We have developed a modified RTM imaging method (the asym-RTM) to image the fault directly. Simply by incorporating a calculated reflector of the traditional RTM image into the smoothed background velocity, we can utilize the second order scattering events to form the fault image in the asym-RTM. In the two numerical examples, we imaged the vertical faults with high fidelity.

6 Conclusions and future work

6.1 Conclusions

In this dissertation, two new algorithms were developed in order to utilize multiply scattered waves to characterize fractures and image faults respectively. For fracture characterization, the Gaussian wave packet (GWP) is chosen to approximate local plane waves and interact with fractures locally. The resultant multiply scattered waves are used to characterize the fractures. For fault imaging, the asymmetrical reverse time migration is proposed to employ second-order scattered waves for imaging the faults directly in the same way as the sub-horizontal reflectors are imaged.

To implement GWP in fracture characterization, we studied its diffraction-resistant property relative to the propagation distance in both homogenous and heterogeneous media. During the process of synthesizing GWP data from the point-shot data, we considered the effects of noise, statics, and point-source intervals on the final synthesized GWP. A local image was produced from the synthesized GWP to demonstrate its directionality and localization along the propagation path. When the GWP was applied to characterize fractures, we did two numerical tests to prove its feasibility. In the first test, three sets of fractures with different spacing at different horizontal locations were recovered. In the second test, two sets of fractures with different spacing at different vertical locations were successfully detected.

In fault imaging, we did three numerical tests to prove the feasibility of the asym-RTM. The first numerical model is a simple step model which is widely used in the literature for fault imaging.

The second numerical model is a vertical fault in horizontal layers. The third one is a high-angle fault in a complex geolocical background. For all these models, we have imaged the fault clearly and correctly using asym-RTM.

6.2 Future work

For fracture characterization, we noticed that the source interval is important to synthesize a proper GWP from the point shot gathers. Seismic data interpolations should be useful before applying the synthesis of GWP. Extending fracture characterization from 2D to 3D needs to be further studied.

In our fracture characterization method, we assume that there is no free surface effect. However, the free surface effect in reality may generate strong multiples, and wave type conversions (P to S and S to P). It will be difficult to process and remove all unwanted waves just based on the pressure data. Due to the improvements in seismic acquisition, we may be able to remove waves caused by the surface effect using recorded data with 4-component receivers. This research direction of free surface effects should be explored too.

The theory and method of asymmetrical reverse time (asym-RTM) migration was proposed at first only for imaging steep faults. It should be easy to apply asym-RTM in salt flank imaging which is a difficult task in traditional seismic imaging.

For both the fracture characterization and fault imaging, further applications with real datasets should be performed.

In traditional seismic imaging, multiply scattered waves are treated as noise and need to be suppressed during preprocessing. Though we only utilized multiply scattered waves in two applications, it is promising to apply multiply scattered waves in many other aspects of seismic imaging.

Bibliography

Babich, V. and V. Ulin (1984). Complex space-time ray method and "quasiphotons". *Journal of Soviet Mathematics 24*(3), 269–273.

Bakulin, A. and R. Calvert (2006). The virtual source method: Theory and case study. *Geophysics 71*(4), SI139–SI150.

Baysal, E., D. D. Kosloff, and J. W. Sherwood (1983). Reverse time migration. *Geophysics 48*(11), 1514–1524.

Candès, E., L. Demanet, D. Donoho, and L. Ying (2006). Fast discrete curvelet transforms. *Multiscale Modeling & Simulation 5*(3), 861–899.

Červenỳ, V., M. M. Popov, and I. Pšenčík (1982). Computation of wave fields in inhomogeneous media—Gaussian beam approach. *Geophysical Journal of the Royal Astronomical Society 70*(1), 109–128.

Chen, L., R.-S. Wu, and Y. Chen (2006). Target-oriented beamlet migration based on Gabor-Daubechies frame decomposition. *Geophysics 71*(2), S37–S52.

Cohen, I., N. Coult, and A. A. Vassiliou (2006). Detection and extraction of fault surfaces in 3d seismic data. *Geophysics 71*(4), P21–P27.

Crampin, S. (1985). Evaluation of anisotropy by shear-wave splitting. *Geophysics 50*(1), 142–152.

da Costa, C. A., S. Raz, and D. Kosloff (1989). Gaussian beam migration. In *SEG Technical Program Expanded Abstracts 1989*, pp. 1169–1171. Society of Exploration Geophysicists.

De Hoop, M. V., J. H. Le Rousseau, and R.-S. Wu (2000). Generalization of the phase-screen approximation for the scattering of acoustic waves. *Wave Motion 31*(1), 43–70.

Douma, H. and M. V. de Hoop (2007). Leading-order seismic imaging using curvelets. *Geophysics 72*(6), S231–S248.

Fang, X., Y. Zheng, and M. C. Fehler (2017). Fracture clustering effect on amplitude variation with offset and azimuth analyses. *GEOPHYSICS 82*(1), N13–N25.

Fishman, L. (2002). Applications of directional wavefield decomposition, phase space, and path integral methods to seismic wave propagation and inversion. *Pure and Applied Geophysics 159*(7), 1637–1679.

Geng, Y., J. Mao, R. Wu, and J. Gao (2012). Local angle domain target oriented illumination analysis and imaging using beamlets. *Chinese Journal of Geophysics 55*(2), 219–228 0898–9591.

Geng, Y., R. Wu, and J. Gao (2014). Gaborframebased Gaussian packet migration. *Geophysical Prospecting 62*(6), 1432–1452.

Hale, D. (2013a). Methods to compute fault images, extract fault surfaces, and estimate fault throws from 3d seismic images. *Geophysics 78*(2), O33–O43.

Hale, D. (2013b). Methods to compute fault images, extract fault surfaces, and estimate fault throws from 3d seismic images. *Geophysics 78*(2), O33–O43.

Hall, C. E., M. Gurnis, M. Sdrolias, L. L. Lavier, and R. D. Müller (2003). Catastrophic initiation of subduction following forced convergence across fracture zones. *Earth and Planetary Science Letters 212*(1–2), 15–30.

He, Y. and R.-S. Wu (2009). Subsalt imaging using secondary scattered waves. In *SEG Technical Program Expanded Abstracts 2009*, pp. 1657–1661. Society of Exploration Geophysicists.

Hernández-Figueroa, H. E., M. Zamboni-Rached, and E. Recami (2007). *Localized waves*, Volume 194. John Wiley & Sons Sons.

Herrmann, F. J. and G. Hennenfent (2008). Non-parametric seismic data recovery with curvelet frames. *Geophysical Journal International 173*(1), 233–248.

Hill, N. R. (1990). Gaussian beam migration. *Geophysics 55*(11), 1416–1428.

Hill, N. R. (2001). Prestack Gaussian-beam depth migration. *Geophysics 66*(4), 1240–1250.

Hu, H. and Y. Zheng (2018a). 3d seismic characterization of fractures in a dipping layer using the double-beam method. *Geophysics 83*(2), V123–V134.

Hu, H. and Y. Zheng (2018b). 3d seismic characterization of fractures in a dipping layer using the double-beam method. *Geophysics 83*(2), V123–V134.

Hu, H., Y. Zheng, X. Fang, and M. C. Fehler (2018). 3d seismic characterization of fractures with random spacing using the double-beam method. *Geophysics 83*(5), M63–M74.

Jerri, A. J. (1977). The Shannon sampling theorem—its various extensions and applications: A tutorial review. *Proceedings of the IEEE 65*(11), 1565–1596.

Kiselev, A. (2007). Localized light waves: Paraxial and exact solutions of the wave equation (a review). *Optics and Spectroscopy 102*(4), 603–622.

Kiselev, A. and M. Perel (1999). Gaussian wave packets. *Optics and Spectroscopy 86*, 307–309.

Kiselev, A. P. (2003). Generalization of Bateman–Hillion progressive wave and Bessel–Gauss pulse solutions of the wave equation via a separation of variables. *Journal of Physics A: Mathematical and General 36*(23), L345.

Kiselev, A. P. and M. V. Perel (2000). Highly localized solutions of the wave equation. *Journal of Mathematical Physics 41*(4), 1934–1955.

Klimeš, L. (1989). Gaussian packets in the computation of seismic wavefields. *Geophysical Journal International 99*(2), 421–433.

Le Pichon, X. and P. J. Fox (1971). Marginal offsets, fracture zones, and the early opening of the north atlantic. *Journal of Geophysical Research 76*(26), 6294–6308.

Li, F., B. Zhang, K. J. Marfurt, and I. Hall (2014). Random noise suppression using normalized convolution filter. In *SEG Technical Program Expanded Abstracts 2014*, pp. 4345–4349. Society of Exploration Geophysicists.

Liu, E., J. A. Hudson, and T. Pointer (2000). Equivalent medium representation of fractured rock. *Journal of Geophysical Research: Solid Earth 105*(B2), 2981–3000.

Liu, Y., X. Liu, A. Osen, Y. Shao, H. Hu, and Y. Zheng (2016). Least-squares reverse time migration using controlled-order multiple reflections. *Geophysics 81*(5), S347–S357.

Lynn, H. and L. Thomsen (1990). Reflection shear-wave data collected near the principal axes of azimuthal anisotropy. *Geophysics 55*(2), 147–156.

Malcolm, A. E., B. Ursin, and M. V. De Hoop (2009). Seismic imaging and illumination with internal multiples. *Geophysical Journal International 176*(3), 847–864.

Mendel, J. (1977). White-noise estimators for seismic data processing in oil exploration. *IEEE Transactions on Automatic Control 22*(5), 694–706.

Moczo, P., J. Kristek, and L. Halada. *The finite-difference method for seismologists* (1st ed.). Bratislava; Slovakia: Comenius University.

Nowack, R. L. (2012). A tale of two beams: an elementary overview of Gaussian beams and bessel beams. *Studia Geophysica et Geodaetica 56*(2), 355–372.

Olsson, O., L. Falk, O. Forslund, L. Lundmark, and E. Sandberg (1992). Borehole radar applied to the characterization of hydraulically conductive fracture zones in crystalline rock. *Geophysical Prospecting 40*(2), 109–142.

Perel, M. V. and M. S. Sidorenko (2007). New physical wavelet 'Gaussian wave packet'. *Journal of Physics A: Mathematical and Theoretical 40*(13), 3441.

Popov, M. (1982). A new method of computation of wave fields using Gaussian beams. *Wave motion 4*(1), 85–97.

Ralston, J. (1982). *Guassian beams and the propagation of singularities*, pp. xiii, 268 p. Studies in Mathematics. Washington, D.C.: Mathematical Association of America.

Rüger, A. (1998). Variation of p-wave reflectivity with offset and azimuth in anisotropic media. *Geophysics 63*(3), 935–947.

Schuster, G., J. Yu, J. Sheng, and J. Rickett (2004). Interferometric/daylight seismic imaging. *Geophysical Journal International 157*(2), 838–852.

Schuster, G. T. and R. Snieder (2009). *Seismic interferometry*. New York; USA: Cambridge University Press.

Silverman, B. W. (2018). *Density estimation for statistics and data analysis*. New York; USA: Routledge.

Thomsen, L. (1995). Elastic anisotropy due to aligned cracks in porous rock. *Geophysical Prospecting 43*(6), 805–829.

Trice, R. (2014). Basement exploration, west of shetlands: progress in opening a new play on the ukcs. *Geological Society, London, Special Publications 397*, SP397. 3 0305–8719.

Wang, B., R.-S. Wu, Y. Geng, and X. Chen (2014). Dreamlet-based interpolation using POCS method. *Journal of Applied Geophysics 109*, 256–265.

Wang, Y. (2006). Inverse q-filter for seismic resolution enhancement. *Geophysics 71*(3), V51–V60 0016–8033.

Wapenaar, K. (2004). Retrieving the elastodynamic Green's function of an arbitrary inhomogeneous medium by cross correlation. *Physical review letters 93*(25), 254301.

Wu, R.-S. (2003). Wave propagation, scattering and imaging using dual-domain one-way and one-return propagators. *Pure and Applied Geophysics 160*(3), 509–539.

Wu, R.-S., L. Chen, and Y. Wang (2002). Prestack migration/imaging using synthetic beam sources and plane sources. *Studia Geophysica et Geodaetica 46*(4), 651–665.

Wu, R.-S., B. Wu, and Y. Geng (2008). Seismic wave propagation and imaging using time-space wavelets. In *SEG Technical Program Expanded Abstracts 2008*, pp. 2983–2987. Society of Exploration Geophysicists.

Wu, X. and D. Hale (2016a). 3d seismic image processing for faults. *Geophysics 81*(2), IM1–IM11.

Wu, X. and D. Hale (2016b). Automatically interpreting all faults, unconformities, and horizons from 3d seismic images. *Interpretation 4*(2), T227–T237.

Wu, X., Y. Shi, S. Fomel, L. Liang, Q. Zhang, and A. Z. Yusifov (2019). Faultnet3d: Predicting fault probabilities, strikes, and dips with a single convolutional neural network. *IEEE Transactions on Geoscience and Remote Sensing*.

Xie, X.-B., S. Jin, and R.-S. Wu (2006). Wave-equation-based seismic illumination analysis. *Geophysics 71*(5), S169–S177.

Yan, R. and X.-B. Xie (2010). *The new angle-domain imaging condition for elastic RTM*, pp. 3181–3186 1052–3812. Society of Exploration Geophysicists.

Žáček, K. (2004). Gaussian packet pre-stack depth migration. In *Society of Exploration Geophysicists 74th Meeting Denver, CO*, pp. 957–960.

Zhang, J., T.-k. Shi, Y. Zhao, and H.-w. Zhou (2014). Static corrections in mountainous areas using Fresnel-wavepath tomography. *Journal of Applied Geophysics 111*, 242–249 0926–9851.

Zheng, Y. (2010). Retrieving the exact green's function by wavefield crosscorrelation. *The Journal of the Acoustical Society of America 127*(3), EL93–EL98.

Zheng, Y., X. Fang, M. C. Fehler, and D. R. Burns (2013). Seismic characterization of fractured reservoirs by focusing Gaussian beams. *Geophysics 78*(4), A23–A28.

Zheng, Y., Y. Geng, and R. Wu (2011). Numerical investigation of propagation of localized waves in complex media. In *International Symposium on Geophysical Imaging with Localized Waves*, pp. 24–28.

Zheng, Y. and Y. He (2010). The far-field approximation in seismic interferometry. In *SEG Technical Program Expanded Abstracts 2010*, pp. 4007–4012. Society of Exploration Geophysicists.

Zheng, Y. and R.-S. Wu (2008). *Theory of transmission fluctuations in random media with a depth-dependent background velocity structure* (1st ed.), Volume 50 of *Advances in geophysics*, pp. 21–41. Amsterdam ; Boston: Academic Press.

Zhou, H. (2014). *Practical seismic data analysis* (1st ed.). New York; USA: Cambridge University Press.

Zhou, H.-W., H. Hu, Z. Zou, Y. Wo, and O. Youn (2018). Reverse time migration: A prospect of seismic imaging methodology. *Earth-Science Reviews 179*, 207–227.

Zuberi, M. and T. Alkhalifah (2014). Generalized internal multiple imaging. *Geophysics 79*(5), S207–S216.